Contents lists available at ScienceDirect

Arabian Journal of Chemistry

journal homepage: www.ksu.edu.sa

Original article

Synthesis, characterization, enzyme inhibition, antioxidant, anticancer and antimicrobial potential of organotin(IV) derivatives of 4-fluorophenoxyacetic acid

Shahnaz Rahim [a], Abdul Sadiq [b], Aneela Javed [c], Awal Noor [d,e], Niaz Muhammad [a,*], Mohammad Ibrahim [a], Sadaf Qayyum [d,e], Khurshid Ayub [f], Nighat Fatima [g], Sehrish Sarfaraz [f], Mohammad Assad [h], Maciej Kubicki [i]

[a] Department of Chemistry, Abdul Wali Khan University Mardan, Mardan 23200, Pakistan
[b] Department of Pharmacy, Faculty of Biological Sciences, University of Malakand, Chakdara, 18000 Dir (L), KP, Pakistan
[c] Atta-ur-Rahman School of Applied Biosciences (ASAB), National University of Sciences and Technology (NUST) H-12 Campus, Islamabad, Pakistan
[d] Department of Chemistry, College of Science, King Faisal University, Al-Hassa 31982, Saudi Arabia
[e] Department of Basic Sciences, Preparatory Year Deanship, King Faisal University, Al-Hassa 31982, Saudi Arabia
[f] Department of Chemistry, COMSATS University Islamabad, Abbottabad Campus, Abbottabad, Pakistan
[g] Department of Pharmacy, COMSATS University Islamabad, Abbottabad Campus, Abbottabad, Pakistan
[h] Department of Biochemistry, Abdul Wali Khan University Mardan, Mardan 23200, Pakistan
[i] Faculty of Chemistry, Adam Mickiewicz University, Uniwersytetu Poznanskiego 8, 61-614 Poznań, Poland

ARTICLE INFO

Keywords:
Organotin(IV) carboxylates
Crystal Structures
Anti-inflammatory
Antidiabetic
Anti-Alzheimer
Antioxidant
Antileishmanial
Anticancer
Antimicrobial

ABSTRACT

Five organotin(IV) derivatives (**1**–**5**) of general formula R_3SnL and R_2SnL_2, where R = C_4H_9 {**1**, and **3**}, CH_3 {**2** and **4**}, C_6H_5 {**5**} and L represents 4-fluorophenoxyacetate ligand were synthesized by the condensation reaction of corresponding organotin(IV) chloride and sodium-4-fluorophenoxyaceate salt in dry chloroform under reflux condition. The elemental analysis has confirmed the expected composition of the complexes. The $\Delta\nu$ values (less than 200 cm^{-1}) calculated from FT-IR spectra revealed bridging/chelating bidentate coordination of the carboxylate ligand to the tin. The single crystal XRD analysis has shown polymeric chain structures for complexes **1** and **2** with bridging bidentate carboxylate ligand connecting tin atoms having trigonal bipyramidal geometry. In complex **3**, the tin atom with chelating anisobidentate ligands adopted a highly distorted octahedral geometry. Quantum chemical studies have shown a good correlation between experimental and theoretically calculated geometric parameters. The Hirshfeld surface and fingerprint plots calculations have shown H…H interactions as the major intermolecular contacts present within the crystal structures of complexes **1**–**3**. The experimental and simulated (^{1}H and ^{13}C) NMR spectra were found to be in good agreement. The *in vitro* enzyme inhibition {acetylcholinesterase (AChE), butyrylcholinesterase (BChE), monoamine oxidase B (MAO-B), alpha-glucosidase, dipeptidyl peptidase-4, cyclooxygenase (COX) and lipoxygenase (LOX)}, antioxidant [DPPH = 2,2-diphenyl-1-picrylhydrazyl and ABTS = 2,2′-azino-bis(3-ethylbenzothiazoline-6-sulfonic acid] and antileishmanial assays have shown dose dependent responses of the test compounds. Complexes have shown higher activities compared to the free ligand acid. Complexes were particularly more active acetylcholinesterase (AChE), and butyrylcholinesterase (BChE) inhibitors, especially complex **3** (IC_{50} = 0.60 μg/mL) was even more potent than the standard drug Galantamine (IC_{50} = 2.82 μg/mL). MTT [MTT= (3-(4,5-dimethylthiazol-2-yl)-2,5-diphenyltetrazoliumbromide tetrazolium)] assay showed potent anticancer activity for complex **4** (IC_{50} = 12.54 ± 0.19 μg/mL), complex **5** (IC_{50} = 16.44 ± 0.17 μg/mL), and free 4-fluorophenoxyacetic acid (**HL**) (IC_{50} = 21.95 ± 0.09 μg/mL) among the tested compounds towards the brain cancer cell line (Malignant glioma U87). The nonmalignant human embryonic kidney HEK293 cells were found to be less vulnerable to the test compounds. In the antimicrobial assays, complexes **1** and **2** have shown activities higher than the standard drug Cefixime against *C. albicans* and *P. aeruginosa*, respectively.

* Corresponding author.
E-mail address: drniaz@awkum.edu.pk (N. Muhammad).

https://doi.org/10.1016/j.arabjc.2024.105698
Received 4 November 2023; Accepted 26 February 2024
Available online 28 February 2024

1. Introduction

Organotin(IV) carboxylates are typically prepared by simple one-step condensation reactions of organotin(IV) chlorides/hydroxides/oxides with carboxylic acids/salts in appropriate organic solvents under reflux conditions. The study of these complexes encompasses a significant portion of the organometallic chemistry and is progressively expanding and gaining interest due to their potential to interact with different biomolecules (Debnath et al., 2024). This interaction makes them an important class of compounds with promising biological activities. Numerous studies have recognized these complexes for their anticancer, DNA binding, antimicrobial, antidiabetic, anti-inflammatory, antimalarial, antituberculosis, antileishmanial, antioxidant, antiviral, and enzyme inhibition activities that are comparable or more promising than standard drugs used in some studies (Kovala-Demertzi et al., 2002, Muhammad et al., 2009, Abbas et al., 2013, Romero-Cháveza et al., 2018, Naz et al., 2019, Debnath et al., 2020, Hussain et al., 2023, Joshi et al., 2023). The biological activity of these complexes could be linked to their structural diversity attained due to the coordination sphere expansion ability of the tin center and the versatile coordination mode of the carboxylate ligand (Abbas et al., 2013, Romero-Cháveza et al., 2018, Pantelić et al., 2021, Debnath et al., 2024, Kasalović et al., 2024). However, the role of the attached alkyl/aryl groups could not be neglected as their number and length have a significant impact on the bioactivity (Muhammad et al., 2018). Organotin(IV) complexes consisting of relatively small semi-rigid and flexible benzene core carboxylate ligands show significant biological activities (Naz et al., 2019). Substitution of different functional groups on the benzene ring of the carboxylate ligand or even changing the position of a functional group on the benzene ring of the carboxylate ligand has a significant impact on the bioactivity (Muhammad et al., 2018, Muhammad et al., 2019a, Naz et al., 2019).

Keeping in view, the easy synthesis, structural diversity, potent bioactivity and our research interest in the organotin(IV) carboxylate chemistry, we report the synthesis and structural characterization of five organotin(IV) derivatives of 4-flourophenoxyacetic acid for their *in vitro* biological activities. As different studies have reported a close connection among oxidative stress, inflammation, cancer, diabetes and Alzheimer's disease (Fernandes et al., 2024, Ojo et al., 2023), so the complexes were screened for their enzyme inhibition (anti-Alzheimer, antidiabetic and anti-inflammatory), antioxidant, anticancer, anti-leishmanial, and antimicrobial activities in search of metal based multifaceted drugs. The characterization of the synthesized complexes was achieved via elemental analysis, FT-IR, NMR (^{1}H and ^{13}C) and single crystal XRD analyses. The ligand acid was selected for its relatively flexible and semi-rigid nature and polar fluoro substituent for efficient bioactivity after complexation with organotin(IV) moiety.

2. Experimental

2.1. Materials and physical measurements

Organotin(IV) chlorides, 4-flourophenoxyacetic acid, sodium bicarbonate and chloroform were purchased from Sigma-Aldrich and used without any further purification. However, chloroform was dried according to a reported procedure (Armarego and Chai, 2003). Melting points of the synthesized complexes were determined on a Gallenkamp (UK) electro thermal instrument. FT-IR spectra given in Fig. S1-S5 were recorded in the range of 4000–400 cm^{-1} on a Nicolet-6700 FT-IR Spectrophotometer, Thermo Scientific, USA, using attenuated total reflectance (ATR) technique. The NMR (^{1}H and ^{13}C) spectra given in Fig. S6-S15 were recorded at room temperature on a Bruker Avance III HD NanoBay 400 MHz NMR spectrometer (Switzerland).

2.2. Syntheses

2.2.1. Sodium-4-flourophenoxyacetate (*NaL*)

The ligand salt, sodium-4-flourophenoxyacetate (**NaL**) was prepared by the drop wise addition of an aqueous sodium hydrogen carbonate solution to an equimolar methanolic solution of 4-flourophenoxy acetic acid. The reaction mixture was stirred for an hour. The soluble sodium-4-flourophenoxy acetate salt was recovered from the solution by rotary evaporation as a white powder.

2.2.2. Synthesis of *1*–*5*

For the syntheses of **1** and **2**, one equivalent of **NaL** (0.5 g, 2.45 mmol) and tri-*n*-butyltin(IV) chloride (0.798 g, 2.45 mmol) or trimethyltin(IV) chloride (0.488 g, 2.45 mmol) were dissolved in 100 mL of dry chloroform in a 250 mL two neck round bottom flask. The reaction mixture was refluxed for 6 h. The resultant turbid solution was cooled to room temperature and left undisturbed for 24 h. The precipitated sodium chloride was removed by filtration. The crude complex was recovered from the clear filtrate by rotary evaporation of the solvent and recrystallized from chloroform and *n*-hexane mixture (4:1). For the syntheses of **3**, **4** and **5**, two equivalents of **NaL** (0.5 g, 2.45 mmol) and one equivalent of di-*n*-butyltin(IV) dichloride (0.372 g, 1.22 mmol), dimethyltin(IV) dichloride (0.269 g, 1.22 mmol) or diphenyltin(IV) dichloride (0.421 g, 1.22 mmol) were used and recrystallized in the same manner as **1** and **2**.

2.3. X-ray single crystal analysis

Diffraction data were collected by the ω-scan technique, at 100(1) K, on Rigaku XCalibur four-circle diffractometer with Eos CCD detector, equipped with graphite-monochromatized MoKα radiation source (λ = 0.71073 Å). The data were corrected for Lorentz-polarization as well as for absorption effects (Agilent Technologies, 2018). The structures were solved with SHELXT (Sheldrick, 2015a) and refined with the full-matrix least-squares procedure on F2 by SHELXL-2013 (Sheldrick, 2015b). All non-hydrogen atoms were refined anisotropically, hydrogen atoms were placed in idealized positions and refined as 'riding model' with isotropic displacement parameters set at 1.2 (1.5 for methyl groups) times Ueq of appropriate carrier atoms. In the structure **2**, one of the difluorophenyl rings is disordered over two positions, rotated approximately by 180°. The site occupation factors for these positions converged at 65.8 (4)%:34.2(4)%. Weak restraints were applied to the shapes of displacement ellipsoids in disordered fragments.

2.4. Hirshfeld surface analysis

The Hirshfeld surfaces and 2D fingerprint plots were generated using Crystal Explorer 17.50 (Turner et al., 2017). The X-ray single-crystal crystallographic information files were used as input files. The default setting used for Hirshfeld Surface/fingerprint generation in Crystal Explorer is as follows: property: none; resolution: High (standard). For fingerprint generation (di vs. de plot) we used: range: standard; filter: by elements and fingerprint filter options is both inside-outside elements including reciprocal contacts. The interactions with normalized contact distance in crystal structure shorter than the sum of the corresponding van der Waals radii of the atoms are highlighted by red spots and the longer contacts with the positive d_{norm} value are represented in blue color.

2.5. Computational methodology

Gaussian09 package was used to perform all the quantum chemical simulations (Caricato et al., 2009), whereas Gaussview and Chemcraft were used to visualize the optimized geometries of the synthesized complexes (**1**–**5**) (Sarfaraz et al., 2022a, Sarfaraz et al., 2022b). Geometry optimization of all studied complexes was performed using B3LYP

functional of density functional theory. Sn atom was assigned with LanL2DZ basis set, whereas basis set used for other atoms were assigned with the 6-31G(d,p) basis set (Danish et al., 2020). B3LYP is a reliable DFT functional which provides a cost effective way for not only geometric optimizations but also frequently adopted for mechanistic studies (Arshad et al., 2015, Mkrtchyan et al., 2021). ^{13}C and ^{1}H NMR analyses were carried out at WP04 functional using GIAO formalism in $CHCl_3$ solvent using tetramethylsilane (TMS) as an internal standard. WP04 is a DFT functional specifically designed to reproduce the experimental NMR results via theory (Sarotti and Pellegrinet, 2012, Rahman et al., 2015).

2.6. Biological assays

2.6.1. Enzyme inhibition assays

2.6.1.1. α-glucosidase assay. The alpha-glucosidase inhibitory activity of the synthesized complexes (**1**–**5**) was performed according to a published procedure with a sight modification (Rahim et al., 2019). Acarbose was used as a standard drug. alpha-glucosidase solution (0.5 units/mL) was made in 0.1 M phosphate buffer (pH 6.90). *p*-Nitrophenyl-α-D-glucopyranoside was used as a substrate solution. Test compound solutions of different concentrations (500, 250, 125, 62.5, 31.25 μg/mL) were prepared in DMSO. The test compound solutions were mixed with the enzyme solutions, and the mixtures were incubated at 37 °C for 15 min. Subsequently, the substrate solutions were mixed with these solutions and the mixtures were again incubated followed by addition of 80 μL sodium carbonate (0.2 M) solution. The mixture solution without alpha-glucosidase was used as a blank solution. The absorption of the solution was measured at 405 nm. The experiments were performed in triplicate. The percent inhibitions and IC_{50} values were calculated.

2.6.1.2. Dipeptidyl Peptidase-4 assay. The inhibitory effect of the synthesized complexes on the Dipeptidyl peptidase-4 (DPP-4) enzyme was evaluated using fluorescent probe based *in vitro* test (Huneif et al., 2022). DPP-4 (recombinant human) and tetraphenylethne-lys-Phe-Pro-Glu (TPE-KFPE) in buffer (HEPES) were treated with the test compounds at 37 °C for 30 min. The 96-well Microplate Reader was used for the assay. The compounds action was assessed at different concentrations (500, 250, 125, 62.5, 31.25 μg/mL). The experiments were performed in triplicate. Urosolic acid was used as standard drug. The IC_{50} values and inhibition (%) was calculated to have an insight about the enzyme inhibition potential of the test compounds.

2.6.1.3. Acetyl and butyrylcholinesterase assays. The synthesized complexes (**1**–**5**) were tested for the acetyl and butyrylcholinesterase inhibition activities in comparison to galantamine reference. Different concentrations (500, 250, 125, 62.25, 31.25 μg/mL) of the test compounds were made in DMSO. Similarly, the Acetylthiocholine iodide (ACTI) and butyrylthiocholineiodide (BCTI) 0.05 mM solutions were also prepared. The enzyme dilutions were made in phosphate buffer (pH 8). The 5,5′-dithiobis-(2-nitrobenzoic acid) (DTNB) and acetyl and butyrylthiocholine iodide solutions (0.05 mM each) were made in distilled water and kept at 8 °C for 15 min. The enzyme solution (5 μL), test compounds (205 μL) and DNTB (5 μL) solution were mixed and incubated for 15 min at 30 °C. The absorption of the mixture was measured at 412 nm. All the solutions without test compounds served as the negative control, and galantamine served as the positive control. The experiments were performed in triplicate. The % inhibitions and IC_{50} values were calculated (Ahmad et al., 2016, Mahnashi et al., 2022).

2.6.1.4. Monoamine oxidase (MAO-B) assay. The microplate assay, as described earlier (Holt et al., 1997) was used with the following modifications to determine MAO-B inhibitory properties of the synthesized complexes **1**–**5**. In a 96-well microplate, 40 μL of the test compound was added to 30 μL potassium phosphate buffer (0.2 M, pH 7.6) and serially diluted. Following this, 40 μL chromogenic solution (1 mM vanillic acid and 2.5 mM 4-aminoantipyrine in 0.2 M potassium phosphate buffer, pH 7.2 and 4U/ml peroxidase) and 120 μL 2.5 mM ptyramine in 0.2 M potassium phosphate buffer (pH 7.2) was added to each well. Absorbance was then read once at 490 nm using an Opsys MR micro-plate reader. Subsequently, 40 μL of the recombinant human monoamine oxidase B (MAO-B 8U/mL) was added to each well of the microplate. The absorbance of the reaction mixture was read at 490 nm seven times every 5 min. Safinamide was used as a standard. Experiments were performed in triplicates. MAO inhibition was calculated by comparing the rates of enzyme reaction of the test compounds with that of a blank containing potassium phosphate buffer according to the following equation:

Inhibition (%) $= 1. - \frac{RR_{sample}}{RR_{control}} \times$ 100where RR_{sample} is the rate of enzyme reaction of the test compounds and $RR_{control}$ is that of the blank.

2.6.1.5. Anticyclooxygenase-2 assay (COX-2). The synthesized organotin(IV) complexes were tested against COX-2 enzyme. The COX-2 (300 units/mL) was activated on ice for 5 min. A 50 μL co-factor containing glutathione, hematin, 1.0 mM and N,N,N',N'-tetramethyl-p-phenylenediamine (TMPD) in a Tris-HCl buffer (pH 8) was added to the activated solution. The mixtures containing test compound solution (20 μL) and activated enzyme solution (60 μL) were maintained at room temperature for 5 min. The addition of 20 μL of arachidonic acid started the enzyme inhibition reaction. The reaction was incubated for 5 min, and absorbance was measured at 570 nm. The experiments were repeated three times. The inhibitions (%) and IC_{50} values were compared with the standard celecoxib (Mahnashi et al., 2022).

2.6.1.6. 5-Lioxygenase assay (5-LOX). This assay was performed with a slight modification in the reported procedure (Mahnashi et al., 2022) against Montelukast as a standard and linoleic acid was used as a substrate. The test compounds were dissolved in phosphate buffer (pH 6.3) followed by the addition of enzyme solution (10,000 unit/μL). The mixture was incubated for 5 min at room temperature followed by the addition of linoleic acid. The mixture was left for 5 min and absorbance was measured at 234 nm. The experiments were performed in triplicate and the inhibitions (%) and IC_{50} values were calculated.

2.6.2. Antioxidant activity

The *in vitro* antioxidant activity of the **HL** and synthesized complexes (**1**–**5**) was performed via DPPH and ABTS assays.

For the DPPH assay on our samples, we used previously published procedure (Huneif et al., 2023). The solution of 2,2 Diphenyl 1 picrylhydrazyl was prepared by dissolving the DPPH (20 mg) in methanol (100 mL). The absorbance was adjusted at 517 nm to 0.75 using UV–visible spectrophotometer. Afterwards, two milliliter solution of DPPH was added to various concentrations of the samples ranging from 500 to 31.25 μg/ml. The mixture of the sample with DPPH was incubated at normal laboratory temperature for fifteen minutes. The absorbance was measured at 517 nm as mentioned in earlier. The experiments were performed in replicate and the detail values are provided in the supporting information. The percent inhibitions of DPPH free radicals were determined by using the following formula;

$$PercentInhibition = \frac{AbsorbanceofStandard - AbsorbanceofSample}{AbsorbanceofControl} \times 100$$

For the *in vitro* ABTS assay, solutions of K_2SO_4 (2.45 mM) and ABTS (7 mM) were prepared and mixed. The mixture was kept in the dark for approximately 16 h. The phosphate buffer (0.01 M, pH 7.4) was used to dilute the ABTS cation solution, and the absorbance value (0.70) was set at 734 nm. The test compounds of different concentrations (500, 250, 125, 62.25, 31.25 μg/mL) were mixed with 3.0 mL of ABTS solution. The decrease in absorption at 734 nm was noticed after one minute for six

minutes. The ascorbic acid was used as a positive control. The experiments were repeated three times and the IC_{50} values and scavenging activities (%) were calculated (Mahnashi et al., 2022).

2.6.3. Antileishmanial activity

Antileishmanial activity was performed on promastigotes form of *Leishmania tropica*, cultivated in a medium (RPMI-1640), supplemented with 1 % antibiotics and 10 % fetal bovine serum (HIFBS) inactivated by heating and incubated at 25 ± 1 °C. Samples stock solutions (10 mg/mL) were made in DMSO.

The assay was done as per reported procedure with a slight modification (Zghair et al., 2016). *Leishmania tropica* promastigotes (1 x 10^5 parasites/well) and test compounds (1000, 500 and 250 µg/mL) were kept in a flat-bottom 96-well microtiter plate. Amphotericin-B (AmB) and plan media with DMSO were employed as positive control and blank, respectively. The plates were kept at 25 ± 1 °C for 72 h. After this, 100 µL of MTT solution was poured to the wells. The plate was again placed for four hours at 31 °C. A 40 µL of DMSO was poured in to wells to solubilize the formazan crystals of MTT. The plates were stirred slowly for 15 min. A microplate reader (Bio Tek™ ELx800) was used to find the absorbance of these plates at 570 nm. Inhibition (%) was then found by using the equation given below:

$$\text{Cell viability}\ (\%) = \frac{meanODofthesample - meanODofthepositivecontrol}{meanODofthenegativecontrol - meanODofthepositivecontrol} \times 100$$

$$\text{Percent inhibition} = (100 - \text{viability})$$

2.6.4. Anticancer activity

U87-Malignant glioma (ATCC-HTB-14™) and Human Embryonic Kidney HEK293 cell lines were obtained from the cell culture bank of Atta-Ur-Rahman School of Applied Biosciences, National University of Science and Technology (NUST), Islamabad, Pakistan. The cells were cultured in Dulbecco's modified Eagle's medium (DMEM) containing 4.5 g/L glucose, 10 % fetal bovine serum (FBS), and 1 % penicillin and streptomycin solution in a humidified incubator set at 37 °C with 5 % carbon dioxide.

MTT assay involves the estimation of the metabolic activity of the living cells and the most common method used for measuring cytotoxicity of any substance. Cytotoxicity is expressed as the concentration of the synthetic compounds that inhibit the growth of cells by 50 % (IC_{50}). The principle behind this assay is the reduction of MTT reagent to insoluble formazan crystals by viable cells, and hence, cellular viability is measured. In the current study, MTT assay was performed to check the cytotoxicity of **HL** and tin complexes **(1–5),** against the human cancerous cell line U87-Malignant glioma and human embryonic kidney (HEK293) as a control. They were added at a density of 1 × 10^3 cells per well in the 96-well culture plate in a humidified incubator having 5 % CO_2 at 37 °C. After 24 h of post plating when the cells were adhered, 100 µL of varying concentrations of test compounds (10, 20, 40, 80, 100, 150 and 200 µg/mL) were added and incubated for 48 h. After 24 h of addition of the drugs, cytotoxicity was checked by adding 5 mg/mL MTT solution prepared in 15 µL of phosphate-buffered saline (PBS) (BIO BASIC CANADA INC.) to each well and incubated for 3 h. Furthermore, supernatant was discarded, and then, 100 µL dimethyl sulfoxide (DMSO) (Sigma-Aldrich) was added to all the wells to dissolve formazan crystals and incubated again for 30 min. The optical density was measured at a wavelength of 550 nm using a micro plate reader (BIO-RAD PR4100). From the obtained data of absorbance, % cell viability was calculated using the following equation (Yousaf et al., 2022, Khan et al., 2023).

$$\%\ \text{age of cell viability} = \left(\frac{A_{sample} - A_{blank}}{A_{control} - A_{blank}}\right) \times 100$$

2.6.5. Antimicrobial activity

The *in vitro* antifungal activity of **HL** and complexes **1**–**5** was screened against two Candida strains (*Candida albicans* ATCC 9002 and *Candida parapsilosis* ATCC 22019). These strains were used to prepare fresh culture before performing anticandidal activity (Kuete et al., 2011). The fungal species were prepared in normal saline. Standard turbidity 100 µL of pre-adjusted fungal culture were used for the preparation of plates of Sabouraud dextrose agar. Standard drug clotrimazole and sample each 5 µL is applied on the sterile disc arranged on media plates. Plates were kept at 30 °C for 48 h and the zone of inhibition around the disc was measured in mm. The experiment was performed thrice.

To test the strength of antibacterial activity in samples, a disc diffusion method was used (Balouiri et al., 2016). Freshly prepared bacterial strains of *S. aureus*, *B. subtilis*, *E. coli* and *P. aeruginosa* were streaked to make lawn on the nutrient agar plates. Test samples 5 µL, cefixime as the reference standard and DMSO as a negative standard, were loaded into complete sterile discs. After 24 h of incubation at 37 °C, the diameter of the sample inhibition zone and standard were measured.

The experiment was performed thrice.

2.7. ADME properties prediction

The best in silico method for the prediction of pharmacokinetics, biophysical, lipophilic and drug-likeness properties of a proposed drug is Swiss-ADME program (https://www.swissadme.ch/) in which the ADME characteristics such as molecular structure, solubility, absorption, excretion and metabolism are explored. The lipid solubility, logical polarity of the surface area (tPSA), solubility (logS), unsaturation ratio based on sp3-hybridized carbon atoms and rotatable bonds were used in the sustainability radar calculation to measure the drug-likeness of the screened compounds. The compound's drug-likeness analysis and compatibility with "Lipinski's Rule of Five" is also determined from the Swiss-ADME program (Daina et al., 2014, Daina et al., 2017, Lipinski et al., 1997, Walters & Murcko, 2002).

3. Results and discussion

3.1. Synthesis

Five organotin(IV) derivatives of 4-fluorophenoxyacetic acid (**HL**) were prepared by the condensation reaction of di- and triorganotin(IV) chlorides with sodium-4-fluorophenoxyacetate in appropriate mole ratio in dry chloroform under reflux condition. The complexes were obtained as a white powder in good yields (84–79 %), found air-stable and soluble in DMSO and chloroform at room temperature. The complexes were recrystallized from chloroform and *n*-hexane mixture (4:1). The elemental analysis confirmed the expected composition and thus purity of the synthesized complexes.

3.2. FT-IR spectroscopy

FT-IR spectra are frequently used for the solid state structural characterization of organotin(IV) carboxylates. The spectra not only confirm the synthesis of these complexes but also give reasonable indications

about the binding mode of the coordinated carboxylate ligand. A broad band in the range 3600–2600 cm^{-1} and strong bands around 1700 and 1200 cm^{-1} owing to O-H, C = O and C-O bonds vibrations are the characteristics of a free carboxylic acid (Muhammad et al., 2019b). The broad band owing to OH bond vibration disappears after complexation, while C = O and C-O bond vibrations of the free carboxylic acid are replaced by a set of two new bands owing to asymmetric and symmetric vibration of the coordinated COO moiety (Eng et al., 2007). The mode of coordination of the carboxylate ligand is decided by the $\Delta\nu$ value (=COO_{asy}-COO_{sym}) (Hussain et al., 2015).

In the present study, the absence of a broad band above 2600 cm^{-1} and the presence of new weak intensity bands in the range 559–461 cm^{-1} in the complexes spectra indicated deprotonation and subsequent coordination of the carboxylate ligand to the tin center (Sirajuddin et al., 2019). The Sn-C bond vibrations were observed as weak intensity bands in the range 585–532. The $\Delta\nu$ values were found less than 200 cm^{-1} showing the bridging/chelating bidentate coordination mode of the carboxylate ligand to the organotin(IV) moiety (Muhammad et al., 2009). The Ar-F vibration was observed as a prominent band in all the synthesized complexes in the range 1204–1193 cm^{-1} (Viola et al., 2022). The FT-IR spectral findings were at least confirmed for complexes **1**–**3** by single crystal X-ray diffraction analysis.

3.3. Single crystal analysis

The crystallographic data as collected by single crystal analysis is presented in Table 1, while important bond lengths and bond angles are shown in Tables 2 and 3, respectively. Single crystal analysis shows that complexes **1** and **2** are polymeric in nature adopting common *trans*-O2SnC3 coordination sphere of the triorganotin carboxylates with trigonal bipyramidal geometry (Figs. 1 and 2, respectively) (Lockhart and Manders, 1986, Mahon et al., 2005). The Sn atom is bonded with the three alkyl carbons and makes a trigonal plane along with two oxygen atoms from the two carboxylate moieties occupying the axial positions. The nature of the bridging is anisotropic, in which tin forms one short [Sn–O 2.200(3) Å in **1** and 2.2309(19) Å in **2**] and one relatively long [Sn–O 2.370(3) Å in **1** and 2.3970(19) Å in **2** and] bond to oxygen. These bond lengths are comparable to other Sn–O bonds found in typical polymeric triorganotin carboxylates, with short (2.120–2.246 Å) and long (2.24–2.65 Å) bonds, respectively [Gul et al., 2024]. The O–Sn–O angles [171.55(10)∘ in **1** and 170.30(7)∘ in **2**] are also comparable to the typical polymeric triorganotin carboxylates (168.6–178.7∘) (Tiekink, 1994, Tariq et al., 2016, Muhammad et al., 2022).

The molecular structure of complex **3** shows that Sn has a coordination number of six and adopts a highly distorted octahedral geometry (may alternately be also described as bicapped tetrahedron with oxygens capping the faces) in which Sn and the atoms of the acetate groups are nearly coplanar (Fig. 3). The acetates are anisobidentate, with Sn-O distances of 2.113 (2) and 2.534 (3) Å, both of which are significantly shorter than the sum of the van der Waals radii (3.68 Å). The Sn-O/Sn-C bond lengths and different angles around tin center in complex **3** are comparable with a previously reported dibutyltin(IV) carboxylate complex (Muhammad et al., 2018).

Quantum chemical studies were also performed to compare the bond lengths and bond angles with those obtained through single crystal structural analysis. The geometric parameters of studied complexes were optimized at 6-31G(d,p) basis set for all atoms except the Sn atom where LanL2DZ basis set was assigned. The optimized geometries of the studied tin complexes (**1**–**5**) are presented in Fig. 4. The comparison of some important bond lengths and bond angles of optimized structures with that of experimental data for complexes **1**–**3** is reported in Tables 2 and 3, respectively. Whereas the important geometric parameters of optimized structures of **4** and **5** are listed in Table 4.

Tables 2 and 3 show that bond lengths and bond angles obtained through the experimental and theoretical analysis correlated nicely. In case of complex **2**, the deviation in the reported bond lengths is observed in the range of 0.01–0.06 Å. In bond length, the maximum deviation is observed for Sn2—O1 (0.06 Å). Whereas the deviation in bond angle is observed in the range of 1.2–8.2°. For complex **1**, almost a similar deviation pattern in geometric parameters is observed as those in complex **2** due to the structural similarity of both complexes. In this case, the deviation in reported bond lengths and angles is calculated in the range of 0.01–0.09 Å and 0.1–8.4°, respectively. Similarly, the simulated complex **3** shows a nice correlation with the X-ray studies parameters.

Table 1
Crystallographic data of complexes **1**–**3.**

Complex	1	2	3
Empirical formula	$C_{40}H_{66}F_2O_6Sn_2$	$C_{11}H_{15}FO_3Sn$	$C_{24}H_{30}F_2O_6Sn$
Formula mass	918.35	332.94	571.19
Temp. (K)	100	298	293
Crystal system	triclinic	orthorhombic	monoclinic
Space group	*P*-1	*Pbca*	*P* 2/*c*
a (Å)	10.3182 (3)	11.2171 (4)	14.2563 (2)
b (Å)	14.1977 (5)	11.6977 (6)	4.99790 (10)
c (Å)	15.8842 (5)	19.7511 (7)	17.8026 (2)
α (°)	108.515 (3)	90	90
β (°)	95.539 (3)	90	94.9480 (10)
γ (°)	98.057 (3)	90	90
Volume ($Å^3$)	2159.94	2590.41	1263.75
Z, Density (Mg/m^{-3}(−|-))	2, 1.412	8, 1.707	2, 1.501
Abs. coefficient (mm^{-1})	1.206	1.975	8.482
F(000)	944.0	1312.0	580
θ range for data collection	−26.726°	−26.785°	−70.742°
Limiting indices	$h = -13 \rightarrow 12$	$h = -14 \rightarrow 14$	$h = -17 \rightarrow 17$
	$k = -17 \rightarrow 17$	$k = -14 \rightarrow 14$	$k = -6 \rightarrow 5$
	$l = -20 \rightarrow 19$	$l = -25 \rightarrow 24$	$l = -21 \rightarrow 21$
Measured reflections	7509	2139	2325
Independent reflections	10,343	9241	10,241
Reflections with I > 2σ(I)	5429	5210	2325
R_{int}	0.0794	0.0632	0.0640
Goodness-of-fit on F^2	0.922	0.821	0.809
Final R indexes [I>= 2σ(I)]	$R_1 = 0.0617$, $wR_2 = 0.1490$	$R_1 = 0.0421$, $wR_2 = 0.1321$	$R_1 = 0.0511$, $wR_2 = 0.1589$
Data/restraints/ parameters	10343/0/793	10219/0/780	10451/0/771
$R[F^2 > 2\sigma(F^2)]$	0.0617	0.0528	0.0611
CCDC No	2,216,717	2,216,715	2,216,716

Table 2
Selected theoretical and experimental bond lengths (Å) of complexes b-**3.**

1			**2**			**3**		
Bond	Theo	Exp	Bond	Theo	Exp	Bond	Theo	Exp
Sn2—C3	2.13	2.14(5)	Sn2—C3	2.13	2.11(4)	Sn2—C5	2.13	2.12(4)
Sn2—C4	2.13	2.13(4)	Sn2—C4	2.13	2.09(4)	Sn2—O3	2.07	2.14(2)
Sn2—C5	2.13	2.13(3)	Sn2—C5	2.13	2.10(4)	Sn2—O4	2.59	2.53(3)
Sn2—O1	2.11	2.20(2)	Sn2—O1	2.17	2.23(2)	O3—C6	1.31	1.28(4)
O1—C6	1.22	1.25(4)	O1—C6	1.29	1.26(4)	O4—C6	1.23	1.23(4)
O7—C6	1.29	1.26(5)	O7—C6	1.22	1.23(4)	–	–	–

Table 3
Selected theoretical and experimental bond angles (°) of complexes **1**–**3.**

1			**2**			**3**		
Bond	Theo	XRD	Bond	Theo	XRD	Bond	Theo	XRD
O1-Sn2-C3	94.3	86.1	O1-Sn2-C3	97.1	86.4	O3-Sn2-O4	55.3	54.8
O1-Sn2-C4	102.3	97.7	O1-Sn2-C4	101.1	90.8	O3-Sn2-C5	110.5	107.7
O1-Sn2-C5	105.1	96.7	O1-Sn2-C5	105.0	96.8	O3-Sn2-O3	82.9	79.62
O1-Sn2-O8	175.1	170.6	O1-Sn2-O8	178.8	170.2	O3-Sn2-O4	55.3	54.8
C3-Sn2-C4	117.3	119.2	C3-Sn2-C4	114.2	119.9	O3-Sn2-C5	106.7	102.2
C3-Sn2-C5	115.6	115.5	C3-Sn2-C5	116.6	117.8	O4-Sn2-C5	87.4	89.2
C3-Sn2-O8	79.55	84.8	C3-Sn2-O8	81.7	84.9	O4-Sn2-O3	55.3	54.8
C4-Sn2-C5	119.6	124.1	C4-Sn2-C5	118.3	122.3	O4-Sn2-O4	164.4	170.7
C4-Sn2-O8	81.0	88.8	C4-Sn2-O8	85.2	89.6	O4-Sn2-C5	85.9	87.7
C5-Sn2-O8	80.7	85.5	C5-Sn2-O8	97.1	94.2	C5-Sn2-O3	106.2	102.2
C6-O8-Sn2	173.1	171.6	C6-O8-Sn2	142.3	137.7	C5-Sn2-O4	85.9	87.7
Sn2-O1-C6	98.2	86.9	Sn2-O1-C6	119.3	130.0	C5-Sn2-C5	129.5	140.7
O8-C6-01	103.9	95.5	O8-C6-01	117.6	125.0	O3-Sn2-O4	55.3	54.8

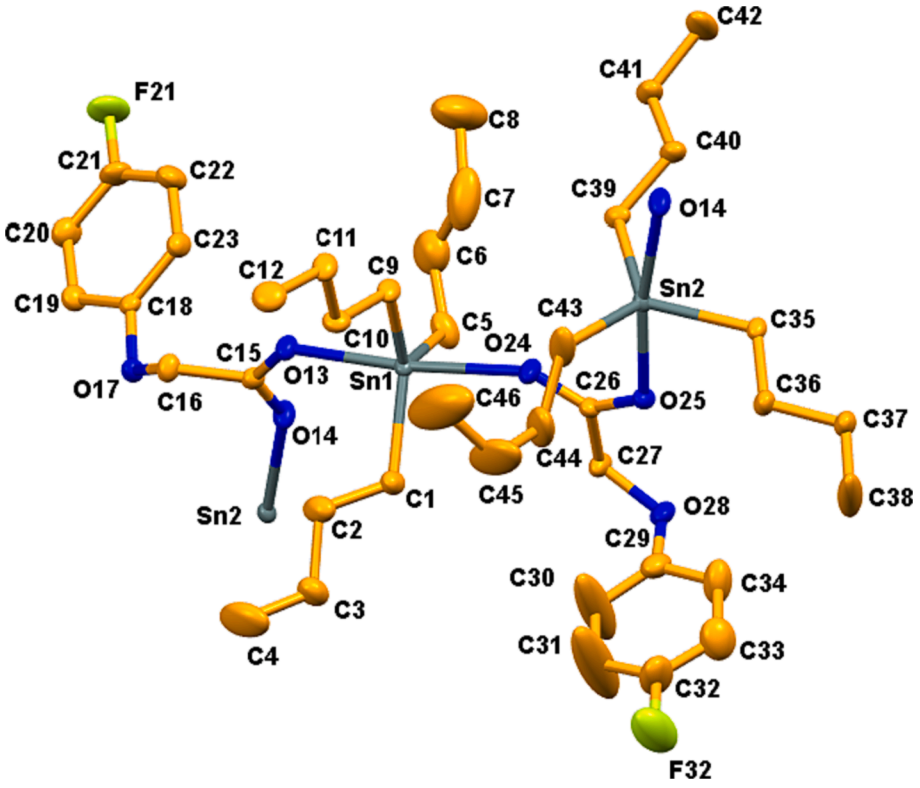

Fig. 1. ORTEP view of **1** with a 50% probability level.

The deviation of simulated bond lengths from that of X-ray results is observed in the range of 0.00–0.07 Å, whereas the deviation in bond angles is in the range of 0.5–7.2°.

Comparative analyses of geometric parameters of complexes **4** and **5** is also indicated and reported in Table 4. Due to missing X-ray results, the selected bond lengths, and angles of complexes **4** and **5** are compared with those of **3**. The geometric parameters for these complexes are almost comparable. The Sn—C bond length of 2.13 Å is observed which is consistent in all simulated complexes (**1**–**5**) as given in Tables 2 and 4. However, Sn—O bond length varies between 2.07 and

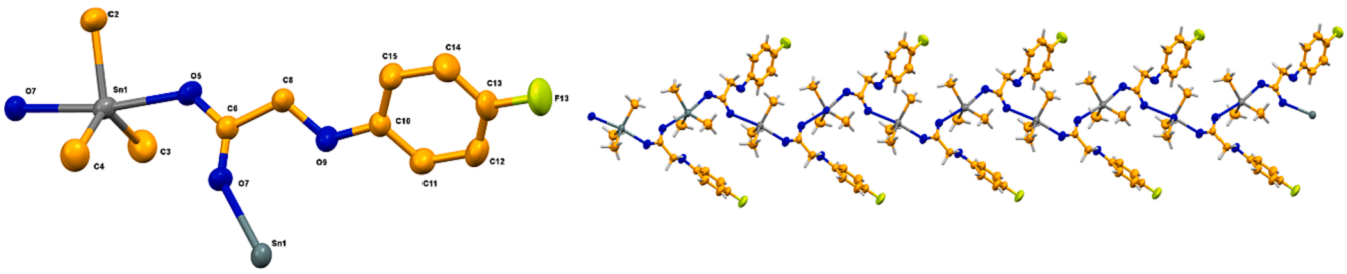

Fig. 2. (Left) ORTEP view of **2** with a 50% probability level (RIGHT) 1-D zigzag polymeric chain structure.

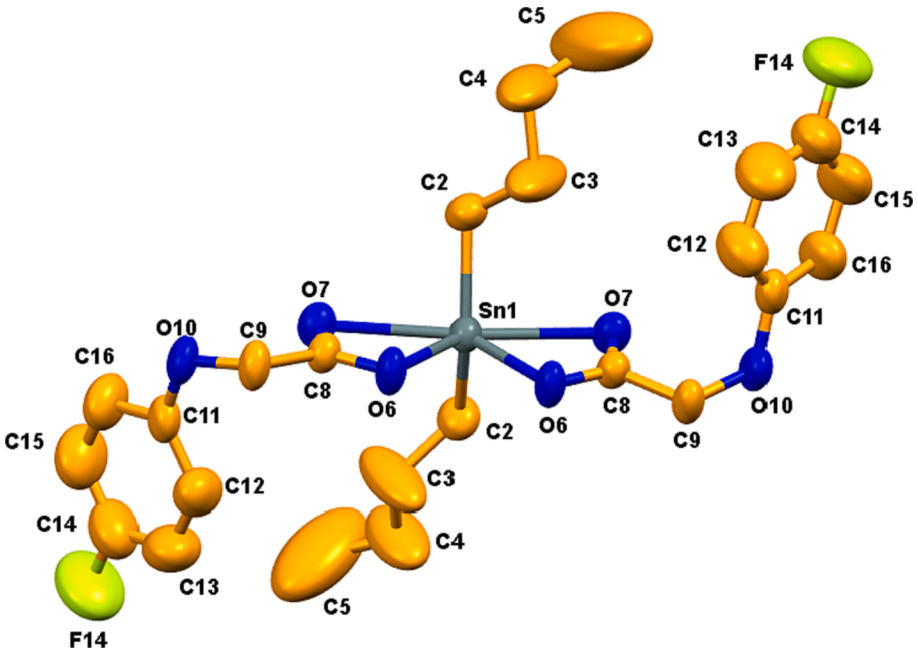

Fig. 3. ORTEP view of **3** with a 50% probability level.

2.64 Å, depending upon the different substituents attached to tin. In summary, the simulated geometric parameters show a very good correlation with those from single crystal X-ray data (experimental) in all tin complexes.

The Hirshfeld surface and fingerprint plots were also calculated to visualize the intermolecular contacts present within the crystal structures of complexes **1**–**3**. The corresponding acceptor and donor atoms showing C—H···O intermolecular hydrogen bonds in complexes **1** and **2** are shown as bright red spots on the Hirshfeld surface (Fig. 5). Both compounds show a maximum proportion of H…H interactions making up 70.5 and 59.5 %, respectively. The higher value for the former could be attributed to the presence of *n*-butyl groups. Despite the fact that the combined C…H/H…C and H…F/F…H contributions dominate the finger plots (12.0 and 10.5 % and 15.3 and 10.0 % for **1** and **2**, respectively), noteworthy are the O…H/H…O interactions of **2** due to H-bonding that can be observed as red circles and are contributing almost twice (14.2 %) than those in **1** (7.7 %) (Figs. 6 and 7).

The Hirshfeld surface and fingerprint plots (Figs. 8 and 9, respectively) show that although in the di-*n*-butyltin(IV) complex (**3**), the intermolecular interactions are still dominated by H…H contacts (54.1 %), the O…H/H…O contacts due to H-bonding are the second most contributions that can be seen as red hot spots. The blue regions correspond to longer contacts with positive d_{norm} value and are evident for H…F/F…H and C…H/H…C interactions (12.2 and 9.6 %, respectively) (Noor, 2022). The white regions correspond to the distance of contacts almost equal to the van der Waals separation with a d_{norm} value of zero and are due to C…F/F…C and O…O contacts (2.2 and 1.2 %, respectively) with no important role in the stabilization of structure (Luo et al., 2013).

3.4. Nuclear magnetic resonance (NMR) spectroscopy

Nuclear magnetic resonance (NMR) spectroscopy has been extensively used in chemistry for the structural elucidation of various compounds. Besides X-ray crystal data, the ^{1}H and ^{13}C NMR chemical shifts give much important information regarding the structures of chemical compounds. The solution state structural characterization of the synthesized complexes was made by ^{1}H and ^{13}C NMR spectra recorded in deuterated chloroform. The numbering scheme for assigning the signals to different protons/carbons is shown in the scheme 1.

In the proton NMR spectra, no signal was observed above 9 ppm, showing the presence of a deprotonated carboxylate ligand in the complexes **1**–**5** (Ali et al., 2021). The shielded part of the complexes (**1**–**4**) spectra is populated by the protons of the alkyl groups attached to the tin atom. The complexes **2** and **4** have shown signals at 0.63 and 1.13 ppm, respectively owing to the methyl protons. The $^{2}J(^{119/117}Sn\text{-}^{1}H)$ coupling constant value of 58/56 suggests a four coordinated tin center in complex **2** in solution form (Ali et al., 2021, Muhammad et al., 2022). The $–CH_2\text{-}CH_2\text{-}CH_2\text{-}$ skeleton of the butyl groups was observed as multiplets in the expected region in complexes **1** and **3** with clear triplets at 0.92 and 0.88 ppm for the terminal CH_3 protons, respectively. The relatively symmetric carboxylate ligand has shown a

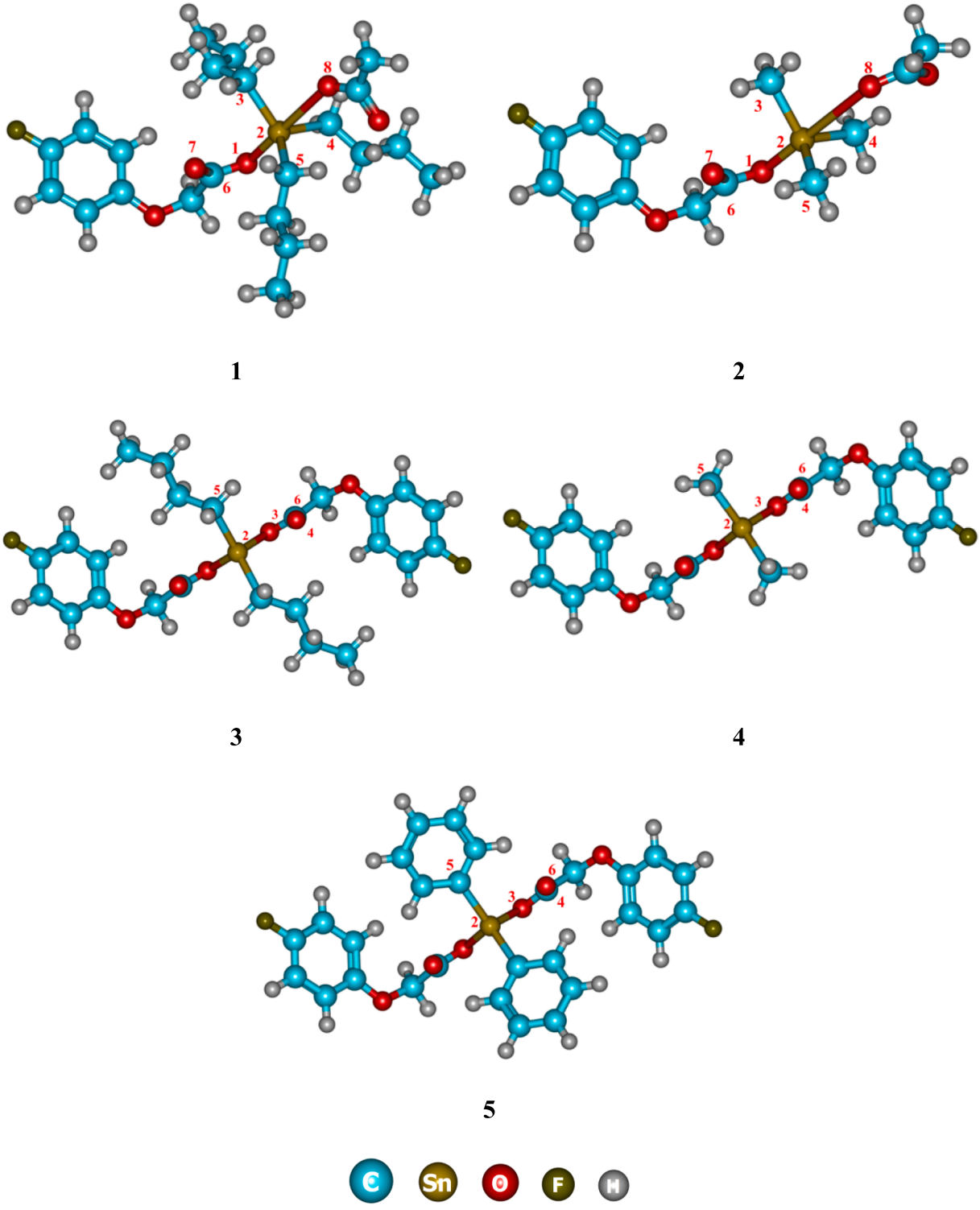

Fig. 4. Optimized geometries of complexes **1**–**5**.

signal owing to the methylene protons in the range of 4.67–4.58 ppm. The aromatic protons of the ligand appeared as two multiplets in the range 6.97–6.82 and 7.53–6.93 ppm.

The ^{13}C NMR spectra of the complexes were relatively simple and gave the signals in the expected regions. Relative analysis of the ^{13}C NMR spectra of the complexes **1**–**5** with **HL** have shown no observable change except an up field/down field shift observed in the COO signal in all the complexes compared to **HL** (173.9 ppm). In case of diorganotin (IV) derivatives (**3** & **4**) a downfield shift was observed, showing a bidentate coordination mode of the ligand. The ligand bidentate coordination deshields the COO moiety, so a downfield signal is observed (Muhammad et al., 2019a). In triorganotin(IV) derivatives (**1** and **2**), an upfield shift was observed for the COO signal due to the monodentate coordination mode of the carboxylate ligand. In a monodentate coordination mode, no significant electronic density transfer occurs from the ligand to the metal center, so the COO moiety remains shielded (Muhammad et al., 2019a). In complex **2**, the tetra-coordinated geometry around tin was further confirmed by the ^{1}J [$Sn^{119/117}$, ^{13}C] coupling

Table 4
Selected theoretical bond lengths(Å) and bond angles(°) of complexes **4** and **5.**

4				**5**			
Atoms	Bond length (Å)	Atoms	Angle (°)	Atoms	Bond length (Å)	Atoms	Angle (°)
Sn2-C5	2.13	O3-Sn2-O4	56.2	Sn2-C5	2.13	O3-Sn2-O4	55.1
Sn2-O3	2.07	O3-Sn2-C5	110.8	Sn2-O3	2.08	O3-Sn2-C5	109.8
Sn2-O4	2.56	O3-Sn2-O3	85.1	Sn2-O4	2.59	O3-Sn2-O3si	80.1
O3-C6	1.31	O4-Sn2-C5	86.8	O3-C6	1.30	O4-Sn2-C5	87.8
O4-C6	1.23	O4-Sn2-O4	162.4	O4-C6	1.24	O4-Sn2-O4	169.6
–	–	C5-Sn2-C5	130.3	–	–	C5-Sn2-C5	130.2

constant value of 394/376 Hz (Muhammad et al., 2019a). The time dependent ^{13}C NMR spectra (taken immediately and after 24 h in $CDCl_3$) have shown no changes in the chemical shift values, thus reflecting the stability of the complexes in solution form.

The quantum chemical DFT calculations play an active role in predicting the simulated NMR chemical shift values and enabling their comparison with the experimental results. The DFT simulations to predict NMR of complexes **1**–**5**, were performed at WP04 functional with 6-31G(d,p) basis set (except LanL2DZ basis set for Sn) using the GIAO method. A comparison of the simulated ^{1}H and ^{13}C NMR chemical shifts with those of the experimental chemical shifts for complexes **1**–**5**, is reported in the experimental section.

All the complexes mainly have methylene, methyl, and aromatic protons. In simulated ^{1}H NMR spectra the methylene protons at position 2 appear in the range of 4.53–4.91 ppm with respect to TMS, whereas these protons in the experimental spectra appear in the range of 4.57–4.77 ppm. Similarly, the aromatic protons at positions 4, 4′ and 5, 5′ are experimentally depicted in the range of 6.87–6.97 and 6.97–7.04 ppm, respectively. The same aromatic protons in the simulated ^{1}H NMR spectra are observed at 6.72–6.82 ppm (4, 4′) and 6.90–7.26 ppm (5, 5′), and are thus very nicely correlated with the experimental results. Moreover, the alpha protons of the methyl group directly attached to the Sn atom are shielded. Thus, the chemical shift values are shifted upfield and appear at 1.03 ppm in simulated and at 1.00 ppm in experimental NMR spectra. Similarly, the simulated and experimental chemical shifts of Hα, Hβ, Hγ and Hσ protons in other studied complexes are correlated excellently as mentioned in the experimental section.

The comparison of simulated and experimental chemical shifts for ^{13}C NMR is also given in the experimental section, and overall, a strong correlation is observed among them. The carbon atom present at position 1 is highly deshielded and appears in the range of 158.5–177.4 ppm (the downfield position). Similarly, in the experimental scan, the chemical shifts of carbon 1 appear in the range of 173.5–178.2 ppm (atomic labeling is according to Scheme 1). The experimental aromatic C4,4′ and C5,5′ signals appeared at 115.6–116.2 ppm, which agree very nicely with the theoretically computed values observed in the range of 111.6–114.9 ppm. The chemical shift of aromatic carbon at position 3 in all tin complexes is observed in the range of 153.7–154.2 ppm, which nicely correlates with the theoretical values appeared in the range of 148.7–152.7 ppm. Similarly, the simulated ^{13}C NMR chemical shift values of all the carbon atoms in complexes **1**–**5** show strong agreement to the experimentally observed chemical shift values. The carbons at alpha position (Cα) attached to Sn are highly shielded in the case of complex **4**, therefore, chemical shifts for Cα appear at slightly upfield positions of 5.3 ppm (experimental) and 13.9 ppm (simulated). Altogether, the simulated ^{1}H and ^{13}C NMR chemical shifts of all the complexes are correlated very nicely with the corresponding experimental values.

3.5. *Biological activities*

3.5.1. *Anti-Alzheimer's assays*

Alzheimer's disease (AD) is a challenging neurological disorder of the elder people. This ailment disrupts daily life activities related to the neurological system (Rizzo et al., 2000). The inhibition of Acetylcholinesterase (AChE), Butyrylcholinesterase (BChE) and Monoamine oxidase B (MAO-B) enzymes are among the major biochemical targets for the management of Alzheimer's disease (Thomas, 2000, Binda et al., 2002, Youdim et al., 2006, Carradori and Silvestri, 2015, Ahmad et al., 2019, Mahnashi et al., 2022).

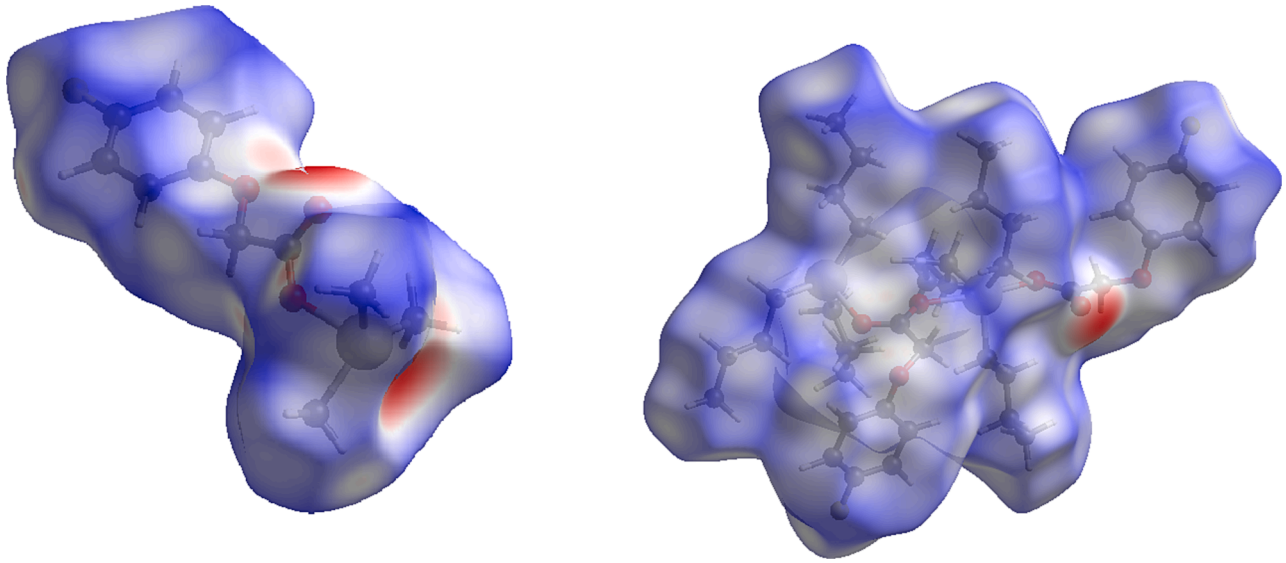

Fig. 5. View of the three-dimensional Hirshfeld surface of **1** (right) and **2** (left) plotted over d_{norm} in the range of − 0.6754 to 1.6747 and − 0.6861 to 1.2194, respectively.

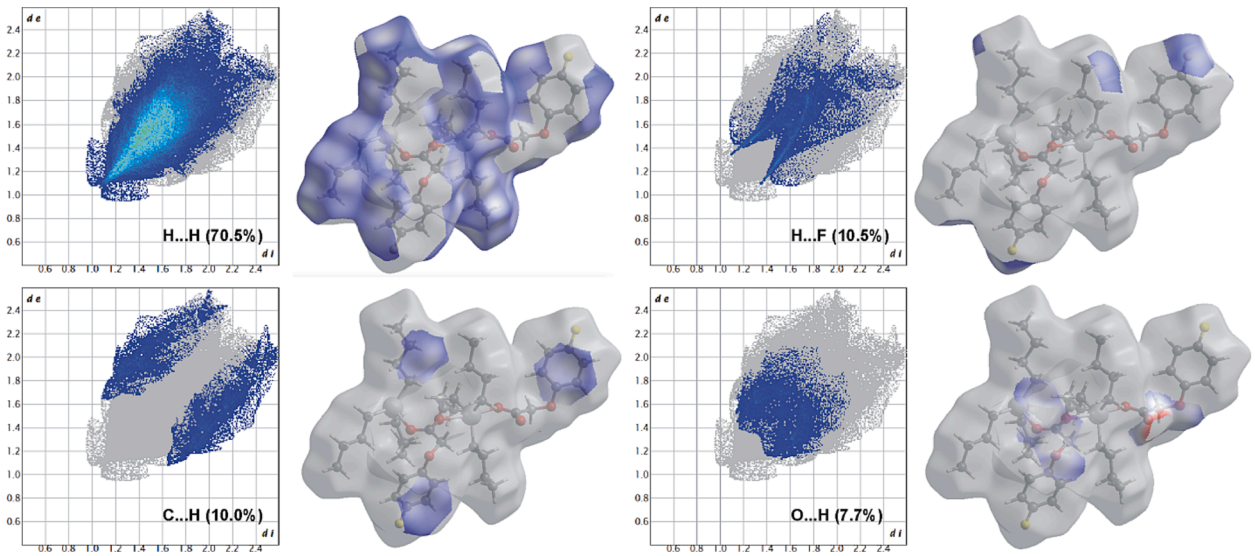

Fig. 6. Two-dimensional finger plots for intermolecular contacts in **1**. The percentage of contribution is specified for each contact.

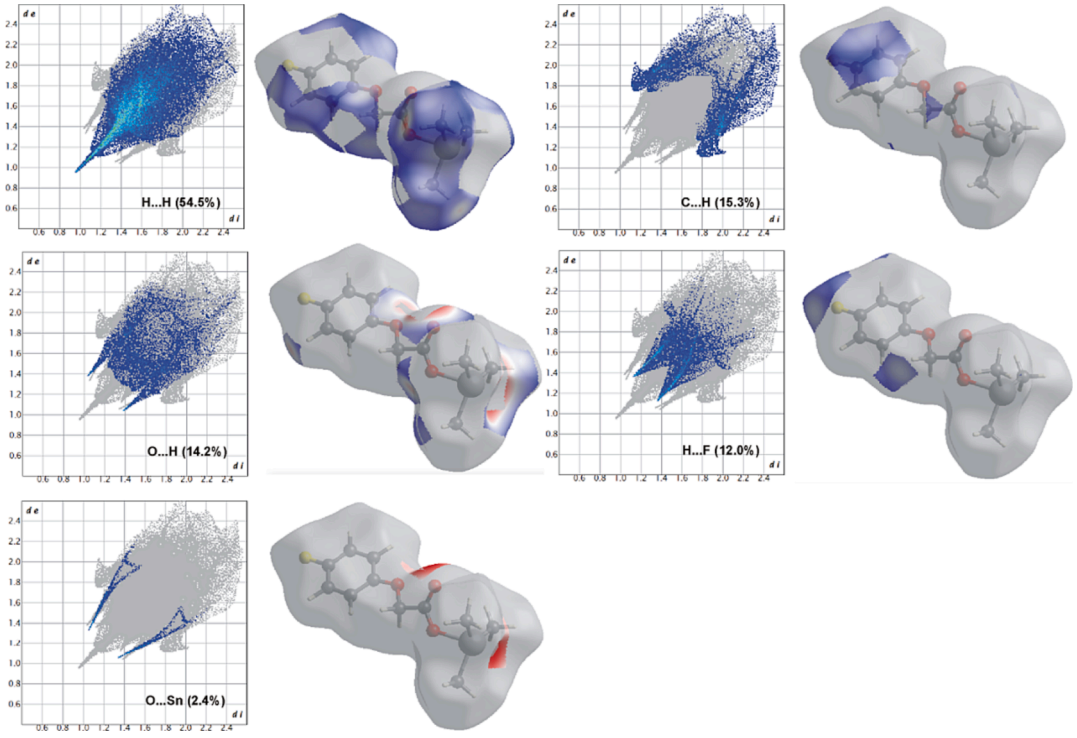

Fig. 7. Two-dimensional finger plots for intermolecular contacts in **2**. The percentage of contribution is specified for each contact.

To evaluate the *in vitro* Anti-Alzheimer potential of **HL** and synthesized complexes **1**–**5,** Acetylcholinesterase (AChE), Butyrylcholinesterase (BChE) and Monoamine oxidase B (MAO-B) were selected as target enzymes. Compounds have shown a dose-dependent response to the target enzymes as shown in Table S1. Complexes **1**–**5** have shown better enzyme inhibition potential compared to **HL**, especially against AChE complexation has increased the enzyme inhibition potential many folds as shown in Fig. 10. Complex **3** with an IC_{50} value of 1.60 μg/mL was even found better enzyme inhibitor than the standard Galantamine. The enhanced activity of the complexes reflects the importance of tin as an active enzyme inhibition center. Complexes have shown different activity orders against the studied enzymes, thus showing different modes of action in these enzymes. Against AChE the activity order **3** > Standard > **4** > **1** > **5** > **2** > **HL** shows that diorganotin(IV) derivatives **3** and **4** are more active than **1** and **2**. Also the complexes with larger alkyl groups are active than complexes with smaller alkyl groups in both di- as well as triorganotin(IV) derivatives. For BChE inhibition complexes have shown different activity order; Standard > **2** > **4** > **1** > **3** > **HL** > **5** as shown in Fig. 10. Against BChE, trialkyltin(IV) derivatives are found more active than their corresponding dilakyltin(IV) analogues. Also, methyl derivatives are more active than butyltin(IV) derivatives. So this activity demanded sterically less hindered tin center for the inhibition potential. In the case of MAO-B, the complexes have shown inhibition potential with no clear controlling factor in the order; Standard > **4** > **1** > **3** > **5** > **2** > **HL** as shown in Fig. 11. Also, complexes were found relatively less potent against MAO-B compared to AChE and BChE. In all

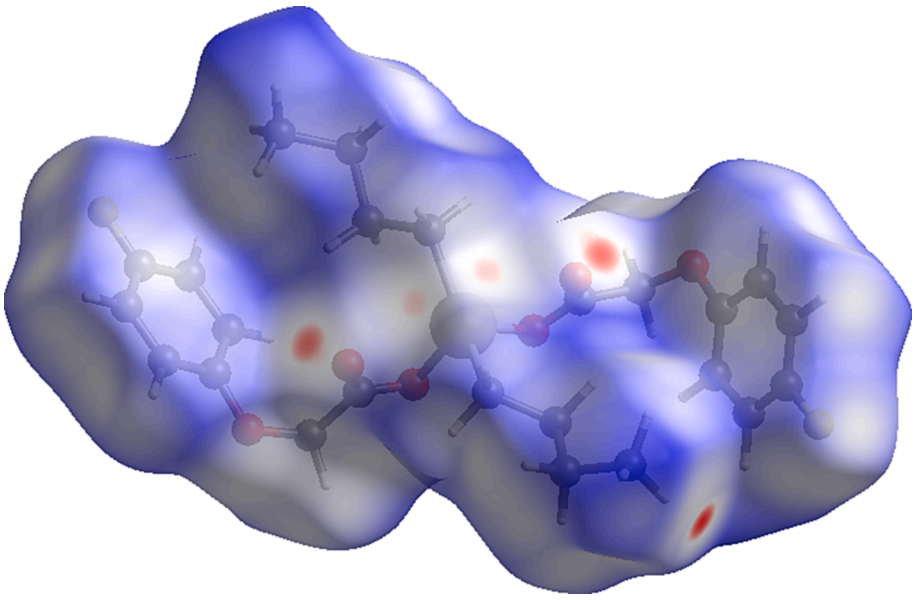

Fig. 8. View of the three-dimensional Hirshfeld surface of **3** plotted over d_{norm} in the range of − 0.2056 to 1.5484.

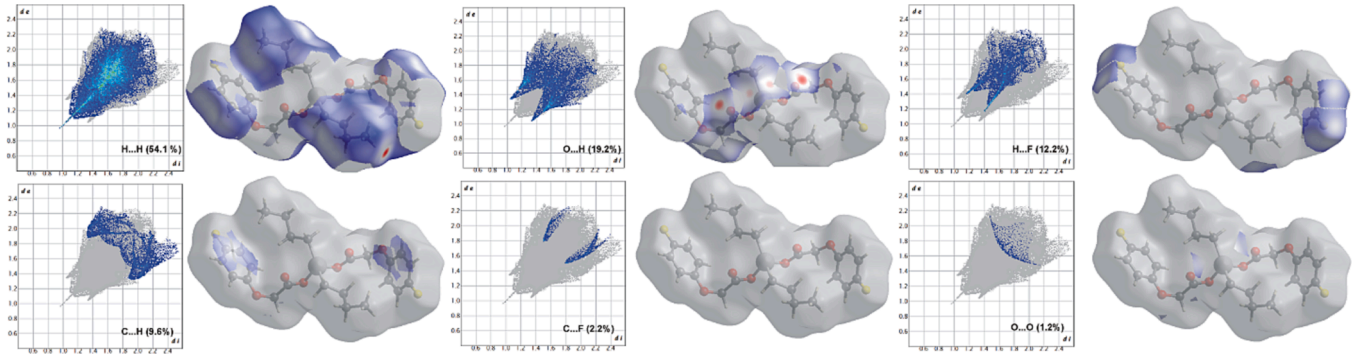

Fig. 9. Two-dimensional finger plots for intermolecular contacts in **3**. The percentage of contribution is specified for each contact.

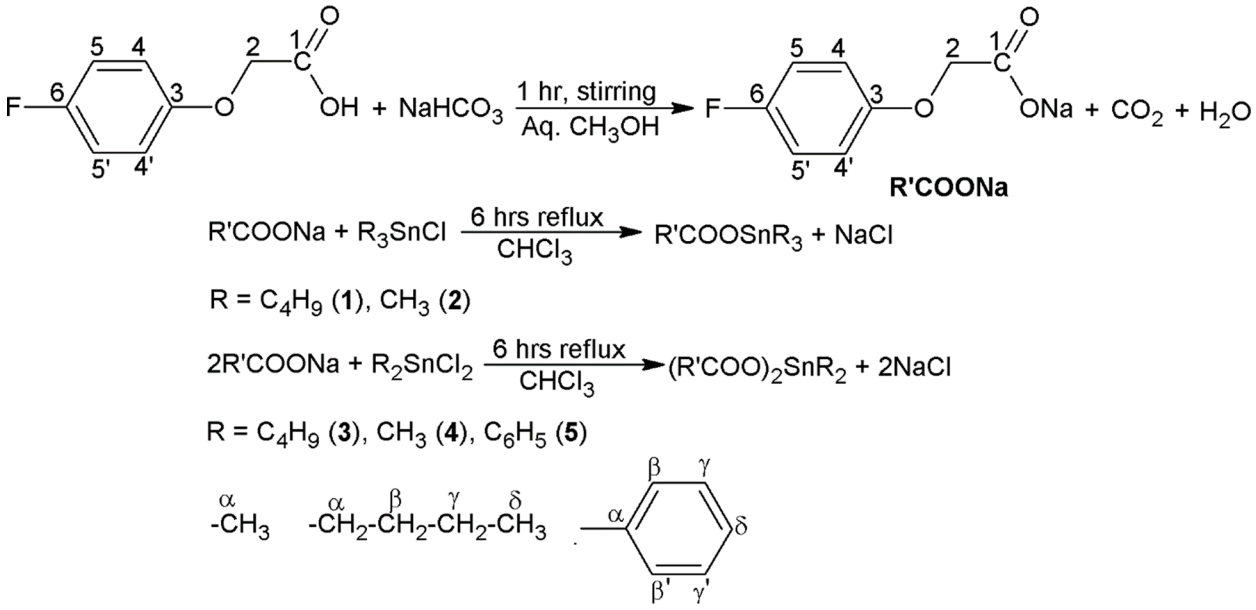

Scheme 1. Synthetic and atomic numbering scheme of complexes **1**–**5.**

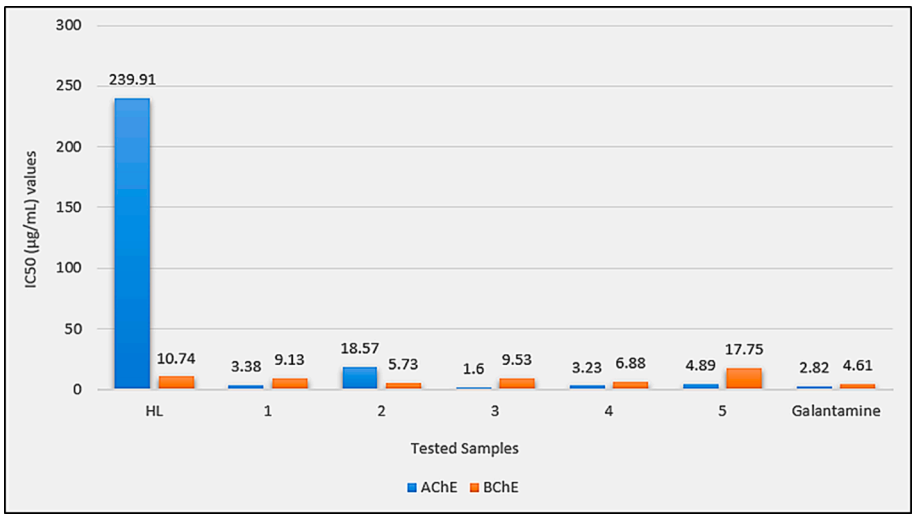

Fig. 10. IC_{50} (µg/mL) values for the *in vitro* Acetylcholinesterase (AChE) and Butyrylcholinesterase (BChE) inhibition assays of **HL** and complexes **1**–**5**.

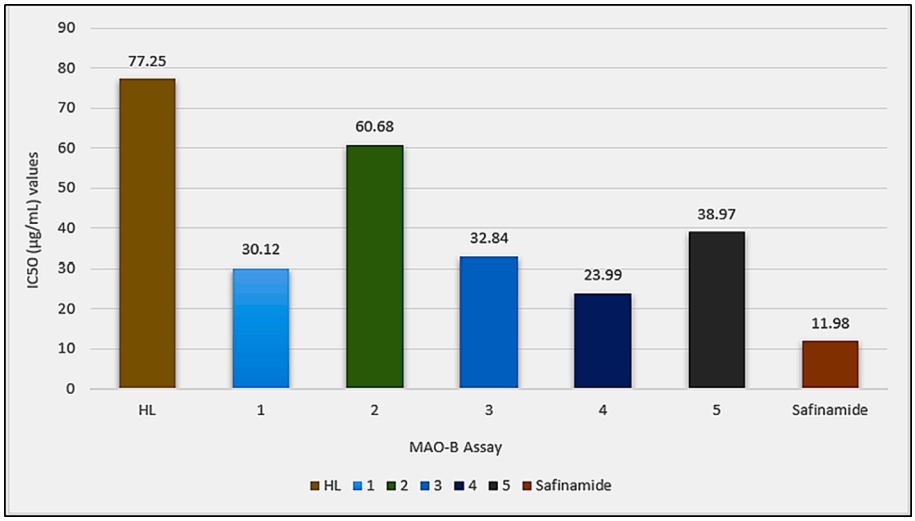

Fig. 11. IC_{50} (µg/mL) values for the *in vitro* Monoamine oxidase B (MAO-B) inhibition assay of **HL** and complexes **1**–**5.**

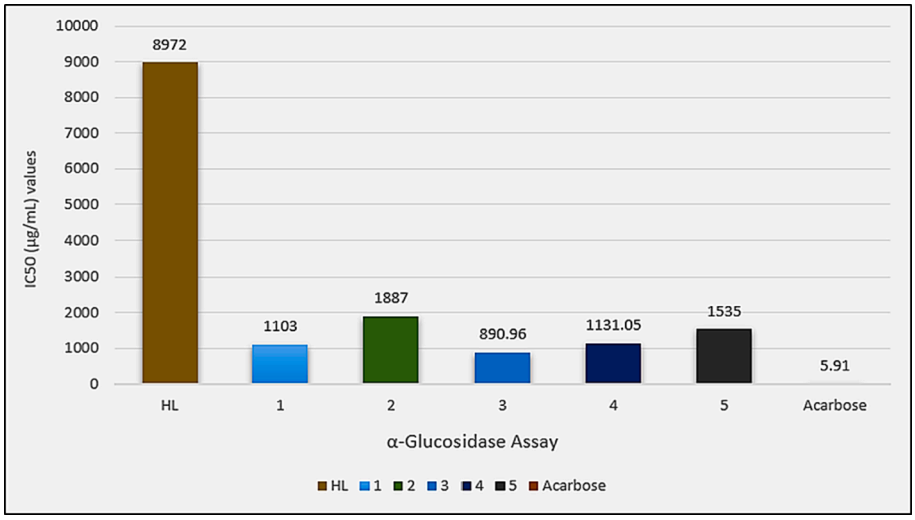

Fig. 12. IC_{50} (µg/mL) values for the *in vitro* alpha-glucosidase inhibition assay of **HL** and complexes **1**–**5**.

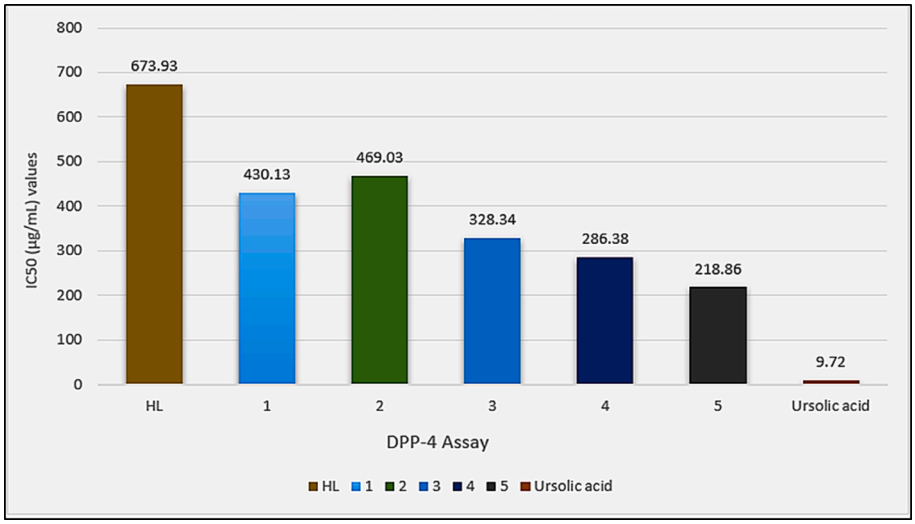

Fig. 13. IC_{50} (µg/mL) values for the *in vitro* DPP-4 inhibition assay of **HL** and complexes **1**–**5**.

three assays, the diphenyltin(IV) derivative (**5**) has shown a relatively low enzyme inhibition potential that could be attributed to the sterically hindered tin center in this complex. The tin atom in complex **5** is not that much freely available for the interaction with the enzyme.

3.5.2. *Antidiabetic assays*

Diabetes mellitus, often known as hyperglycemia, is a metabolic disease associated with high blood sugar levels (Su et al., 2023). Enzymes like alpha-glucosidase and dipeptidyl peptidase-4 (DPP-4) are the main biological targets to treat hyperglycemia (Mahnashi et al., 2021, Mahnashi et al., 2022). Alpha-glucosidase is involved in the digestion of carbohydrates, while DPP-4 has the ability to cleave glucagon-like peptide-1 incretin hormone involved in the proper glycemic control.

The *in vitro* antidiabetic inhibition of **HL** and synthesized complexes (**1**–**5**) was evaluated against alpha-glucosidase and DPP-4 enzymes in comparison to acarbose and ursolic acid as standard drugs and the IC_{50} values of the *in vitro* screening are depicted in Figs. 12 and 13, respectively. A dose-dependent response was observed as can be seen in Table S2. Complexation of the ligand has significantly increased the enzyme inhibition potential, especially in the case of alpha-glucosidase inhibition assay. However, complexes have lesser enzyme inhibition potential as shown by their quite higher IC_{50} values compared to the standard drugs. In the alpha-glucosidase inhibition assay, diorganitin (IV) derivatives (**3** and **4**) superseded their triorganotin(IV) analogues (**1** and **2**). Also, the *n*-butyl derivatives (**1** and **3**) were more active than the methyl derivatives (**2** and **4**). Among complexes, diphenyltin(IV) derivative (**5**) was found better inhibitor than **2**.

Against DPP-4, complex **5** was found active among all complexes. Also, diorganotin(IV) derivatives (**3**–**5**) are found more potent than triorganotin(IV) derivatives (**1** and **2**).

3.5.3. *Anti-inflammatory assays*

The cell or tissue damage is auto-protected from viral, microbial, chemical, or physical injury by the process of inflammation (Hold and El-Omar, 2008). The arachidonic acid pathways play a crucial role in the mechanism of inflammation. The cyclooxygenase (COX) and lipoxygenase (LOX) metabolize arachidonic acid into prostaglandin and leukotrienes (Munir et al., 2020). Prostaglandin and leukotrienes are involved in the inflammatory process (Salmon and Higgs, 1987). The inhibition of COX and LOX enzymes decreases the prostaglandin and leukotriene levels and hence there are lesser chances of inflammation.

The *in vitro* anti-inflammatory assays were performed with cyclooxygenase (COX-2) and lipoxygenase (5-LOX) enzymes using Celecoxib and montelukast as standard drugs, respectively. The test compounds

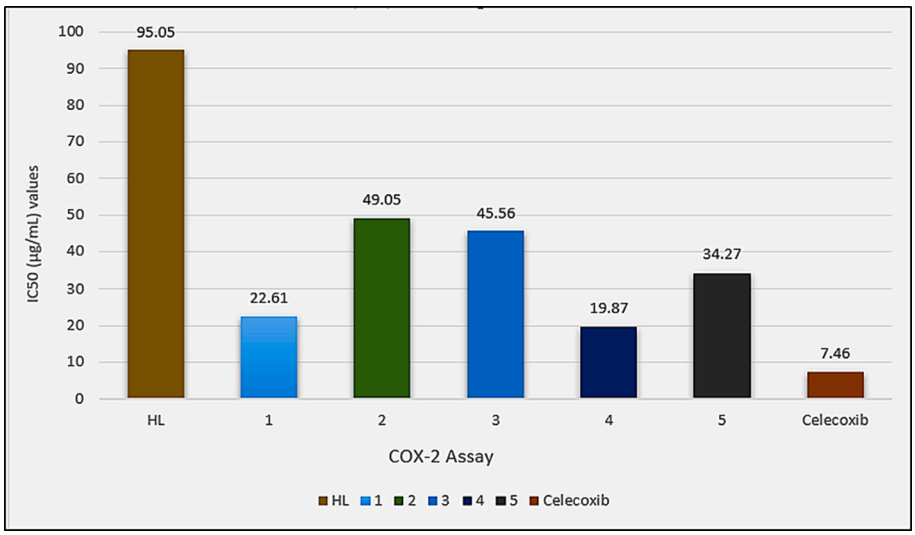

Fig. 14. IC_{50} (µg/mL) values for the *in vitro* cyclooxygenase (COX-2) inhibition assay of **HL** and complexes **1**–**5**.

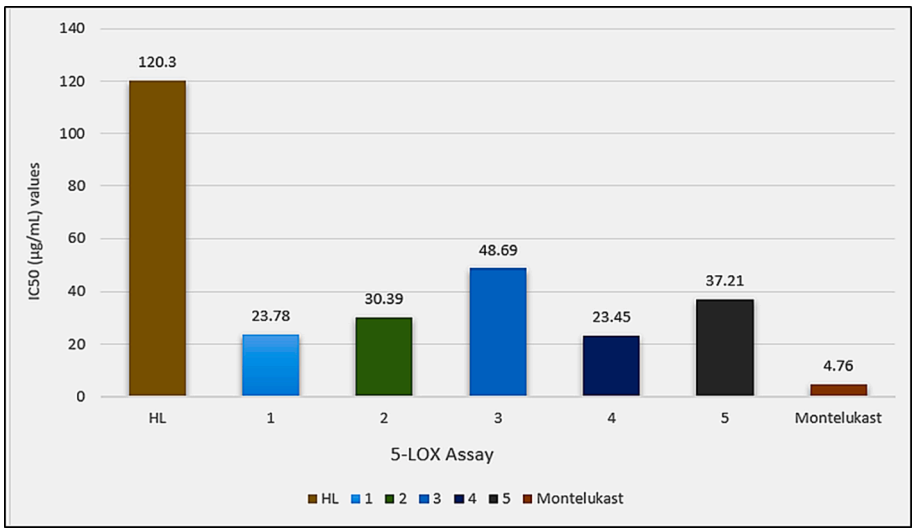

Fig. 15. IC_{50} (µg/mL) values for the *in vitro* lipoxygenase (5-LOX) inhibition assay of **HL** and complexes **1**–**5**.

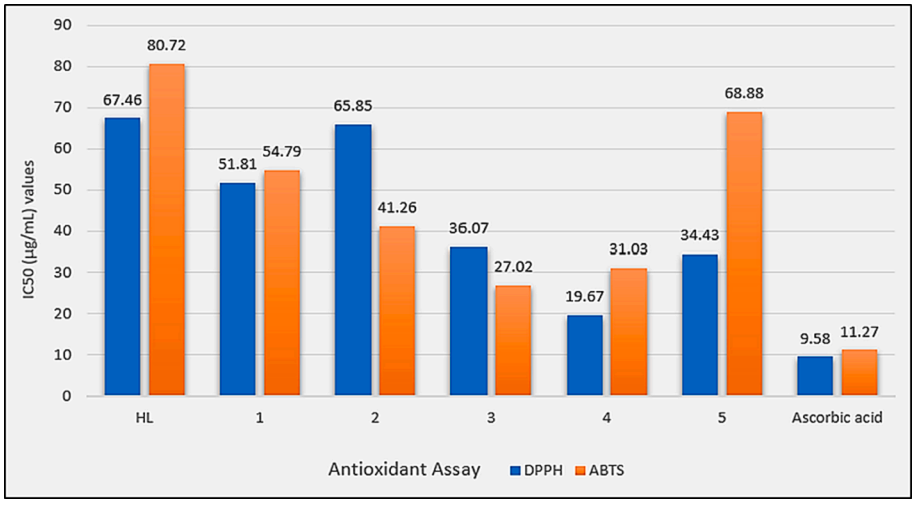

Fig. 16. IC_{50} (µg/mL) values for the *in vitro* antioxidant assays (DPPH, ABTS) of **HL** and complexes **1**–**5**.

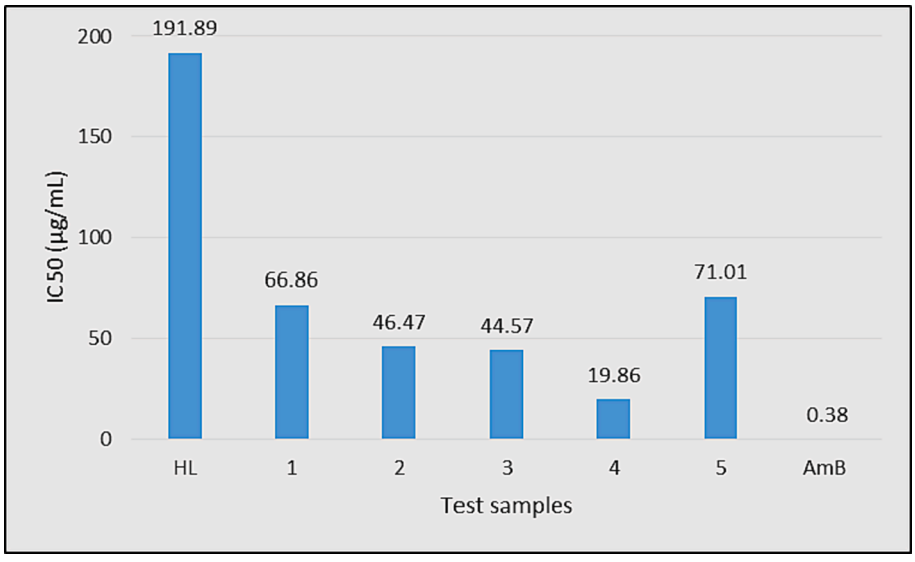

Fig. 17. IC_{50} (µg/mL) values of **HL** and complexes **1**–**5** against L. tropica promastigotes.

have shown a dose (500, 250, 125, 62.5 and 31.25 μg/mL) dependent response towards both the enzymes as shown in Table S3. The complexes have IC_{50} values in the ranges 49.05–19.87 μg/mL and 48.69–23.45 μg/mL against COX-2 and 5-LOX enzymes as shown in Figs. 14 and 15, respectively. These values show higher enzyme inhibition potential of the complexes than **HL** with IC_{50} values of 95.05 μg/mL and 120.3 μg/mL against COX-2 and 5-LOX enzymes, respectively. The test compounds, however, have shown lesser enzyme inhibition potential than the standard drugs Celecoxib and Montelukast with IC_{50} values of 7.46 μg/mL and 4.76 μg/mL, respectively. Among the complexes highest activity was shown by dimethyltin(IV) derivative (**4**) with IC_{50} values of 19.87 μg/mL and 23.45 μg/mL against COX-2 and 5-LOX enzymes, respectively.

3.5.4. *Antioxidant assays*

The overproduction of free radicals could result in oxidative stress, diabetes, cancer, analgesia, inflammation and Alzheimer's disease (Retz et al., 1998). Natural/synthetic antioxidants safeguard human health by quenching the excessive free radicals within the body.

To check the potency of the synthesized complexes as multi-target drugs, the *in vitro* antioxidant potential of **HL** and synthesized complexes (**1**–**5**) was tested by using DPPH and ABTS assays against ascorbic acid as a standard drug and the experimental data are shown in Fig. 16 and Table S4. **HL** with IC_{50} values of 67.46 μg/mL and 80.72 μg/mL against DPPH and ABTS, respectively was found least potent antioxidant agent among the tested compounds. In both the assays dilakyltin(IV) derivatives were found more active free radical scavengers compared to their trialkyltin(IV) analogues, However, diphenyltin(IV) derivative (**5**) was found least potent against ABTS among all complexes. Apart from the number of alkyl groups and coordination number, the length of the alkyl group seems an important factor to affect the free radical scavenging potential of the tested complexes. Dimethyltin(IV) derivative (**4**) was the most active DPPH free radical scavenger. However, against ABTS dibutyltin(IV) derivative (**3**) superseded complex **4**. This activity reversal could be a consequence of different modes of action of the antioxidant in the two assays. The synthesized complexes have shown relatively better antioxidant potential compared to the previously reported organotin(IV) carboxylates (Hussain et al., 2023).

3.5.5. *Antileishmanial activity*

Leishmaniasis is a tropical disease caused by the blood-borne flagellated protozoa of the genus *Leishmania*. Currently, available treatments are relatively less effective, associated with high costs, and have a variety of side effects (Hussain et al., 2023). Therefore, the discovery of new safe alternatives is an urgent need. In this context, **HL** and the synthesized complexes (**1**–**5**) of varying concentrations (250, 500 and 1000 μg/mL) were tested against *L.tropica* promastigotes using MTT assay and the data is shown in Fig. 17 and Table S5. Amphotericin B (AmB) was used as a standard drug. Among the tested compounds, **HL** was found relatively less active with an IC_{50} value of 191.89 μg/mL as shown in Fig. 17. The tin complexes (**1**–**5**) have shown higher activity with IC_{50} values in the range of 71.01–19.86 μg/mL. The higher antileishmanial activity of the complexes compared to **HL** could be a consequence of higher charge distribution and compatibility of the complexes structures to the cell membrane enzyme, trypanothione synthetase (Hussain et al., 2023). Dilakyltin(IV) derivatives were found more active than triakyltin(IV) complexes. Also, dimethyltin(IV) derivative (**4**) was found more active than di-*n*-butyltin(IV) complex (**3**). Similarly, trimethyltin(IV) complex (**2**) was more potent than tri-*n*-butyltin(IV) derivative (**1**). Among the complexes, diphenyltin(IV) derivative (**5**) was found the least active complex with an IC_{50} value of 71.01 μg/mL. The activity pattern suggests that tin complexes with higher coordination numbers and with smaller alkyl groups are more active antileishmanial agents than low-coordinated tin complexes with larger alkyl or aryl groups.

3.5.6. *Anticancer activity*

Different concentrations (10, 20, 40, 80, 100, 150 and 200 μg/mL) of **HL** and synthesized complexes (**1**–**5**) in DMSO were used to investigate the growth inhibition of cancer cells in the human brain cancer cell line (Malignant glioma U87). Simultaneously, human normal embryonic kidney cells (HEK293) were also used in the experiment as a positive control. To ascertain the reduction in cancer cell viability brought on by cytotoxic drugs, the MTT assay was utilized. For Human Malignant glioma U87, the IC_{50} values, and %cell viability of the tested compounds is presented in Fig. 18 and Table S6, respectively. A dose-dependent anticancer response has been noticed. With a rising concentration of the test compounds, a sharp reduction in the viability percentage of the cells was observed. However, at higher drug doses, the %survival decrease of the cells was relatively low.

Results of the MTT assay revealed that all compounds showed good to potent anti-proliferative activity in malignant glioma U87 cells with IC_{50} values in the range of 12.54 ± 0.05 to 142.22 ± 0.04 μg/mL. Among the test compounds, complex **4** (IC_{50} = 12.54 ± 0.19 μg/mL), **5** (IC_{50} = 16.44 ± 0.17 μg/mL) and **HL** (IC_{50} = 21.95 ± 0.09 μg/mL) exhibited the highest inhibitory potency towards the brain cancer cell line (Malignant glioma U87). Human embryonic kidney HEK293 cells were also exposed to the compounds at varying concentrations (10, 20,

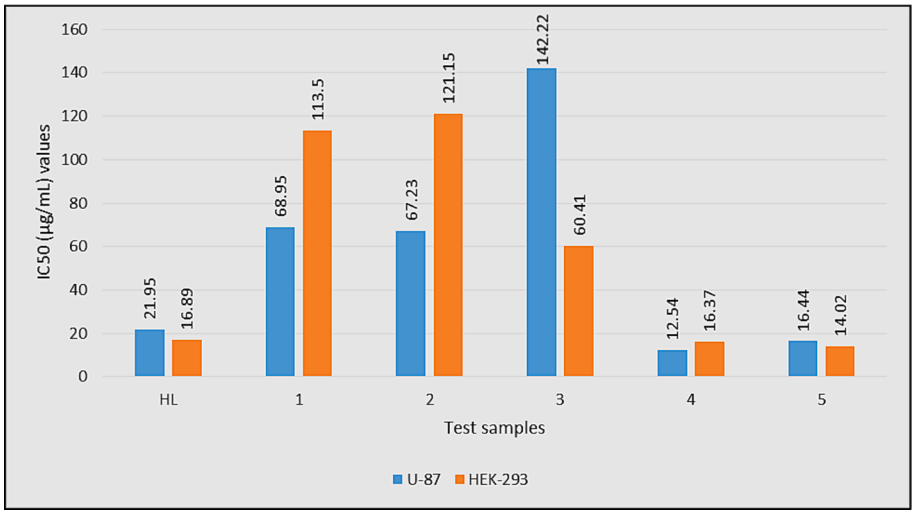

Fig.18. IC_{50} (μg/mL) values of **HL** and complexes **1**–**5** against brain cancer (U-87) and normal (HEK-293) cell lines.

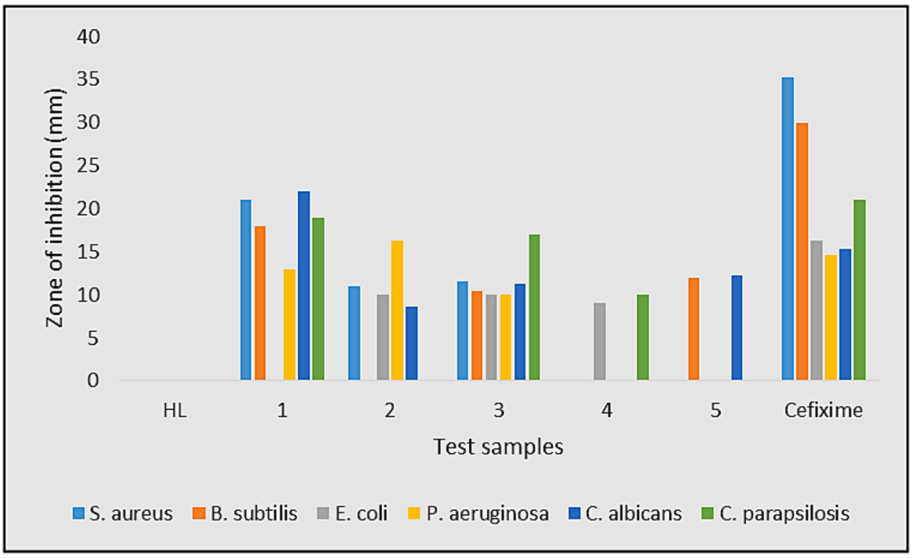

Fig. 19. Antimicrobial activity of **HL** and complexes **1**–**5**.

40, 80, 100, 150 and 200 μg/mL) like the cancer cells to examine the selective cytotoxic effects of the compounds towards malignant cells as compared to the non-malignant cells. The findings suggest that these cells (HEK293) are less vulnerable to the activities of the compounds, particularly complexes **4**, **5**, and **HL**, which increases the death of brain cancer cells. It is observed that the aggressive brain cancer cell line (Malignant glioma U87) responded more positively to the majority of the chemicals with higher cytotoxicity. The lower cytotoxicity of compounds (**4**, **5**, and **HL**) in non-cancerous cells suggests that these novel compounds will provide promising treatment/therapy for patients with brain cancer as suggested earlier (Ahmad et al., 2020). Furthermore, the remaining three complexes (**1**–**3**) were found moderate to less active with IC_{50} values of 68.95 ± 0.01 μg/mL, 67.23 ± 0.08 μg/mL, and 142.22 ± 0.21 μg/mL, respectively. The number and nature of tin bonded alkyl/aryl groups could be considered as the controlling factors for the anticancer activity of the synthesized complexes in the present study. Diorganotin(IV) complexes with smaller methyl (**4**) or planner phenyl (**5**) group are found more active anticancer agents than triorganotin(IV) derivatives. Overall, the synthesized complexes have shown superior anticancer activity compared to the recently reported organotin(IV) carboxylates (Hanifa et al., 2022).

3.5.7. Antimicrobial assays

HL and synthesized organotin(IV) complexes (**1**–**5**) were screened for *in vitro* antibacterial activities against *Escherichia coli*, *Staphylococcus aureus*, *Pseudomonas aeruginosa*, and *Bacillus subtilis*. *Candida albicans* and *Candida parapsilosis* were used for testing the antifungal activity. The *in vitro* antimicrobial results are presented in Fig. 19 and Table S7. **HL** was inactive against any bacterial or fungal strain; however, complexes have shown antimicrobial potency against the selected microbes with some exceptions. Among the test compounds, complexes **1** and **2** have shown activities higher than the standard drug Cefixime against *C. albicans* and *P. aeruginosa*, respectively. These promising results of complexes **1** and **2** render them efficient anti-*C. albicans* and *P. aeruginosa* agents and requires further studies. The higher antifungal activity of tributyltin(IV) derivative (**1**) compared to the trimethyltin (IV) derivative (**2**) has endorsed the previously reported antifungal activity pattern of triorganotin(IV) carboxylates (Ahmad et al., 2020). The test compounds have shown comparable antimicrobial activity with previously reported structurally related organotin(IV) carboxylates (Gul et al., 2024, Muhammad et al., 2022).

3.6. ADME analysis

The ADME (adsorption, distribution, metabolism and excretion) analysis was carried out for **HL** and complexes **1**–**5**, and the data is given in Table 5. The calculated parameters are correlated with drug-like properties and define the relationship between the pharmacokinetic and physicochemical properties of the compound, keeping in view the Lipinski's Rule of Five (Lipinski et al., 1997), an orally-active compound should follow the rule and should not have more than one violation.

The drug recommended range of molecular weight is 130–725 g/mol – all the tested compounds lie within the range. Similarly, the number of hydrogen bond acceptor and donors for the screened compounds lie within the recommended ranges of 2–20 and 0–6, respectively. The ligand **HL** and **2** & **4** have the rotatable bond values in the allowed range, that is, < 10, while **1**, **3**, **5** show violations of this limit. The total polar surface area (tPSA; $Å^2$), used for the determination of drug transport ability (Daina et al., 2017) with smaller tPSA values, < 136 to 157 $Å^2$, indicating greater drug transport ability; all the tested compounds lie in the recommended range. Lipophilicity (logP) is an important drug parameter in measuring the ability of a drug to be dissolve in lipids/oils/fats and non-polar solvents (n-hexane, toluene), (Lobo, 2020, Waring, 2010) and the drug recommended range of

Table 5
In silico properties for **HL** and complexes **1**–**5** determined by SwissADMET.

Comp.#	MW	tPSA	HBD	HBA	RB #	LogP	LogS(ESOL)	LogS(Ali)	Vio.
HL	170.14	46.53	3	4	3	1.55	−2.10	−2.23	0
1	459.17	35.53	0	4	14	4.85	−6.74	−8.20	0
2	332.93	35.53	0	4	5	2.11	−3.96	−3.76	0
3	571.19	71.06	0	8	16	4.70	−7.39	−8.94	1
4	487.03	71.06	0	8	10	2.91	−5.53	−5.98	0
5	611.17	71.06	0	8	12	4.30	−7.94	−8.66	2

tPSA: total polar surface area; HBD: H-bond donor; HBA: H-bond acceptor; RB: Rotatable bond; Vio: Violation from rule of five.

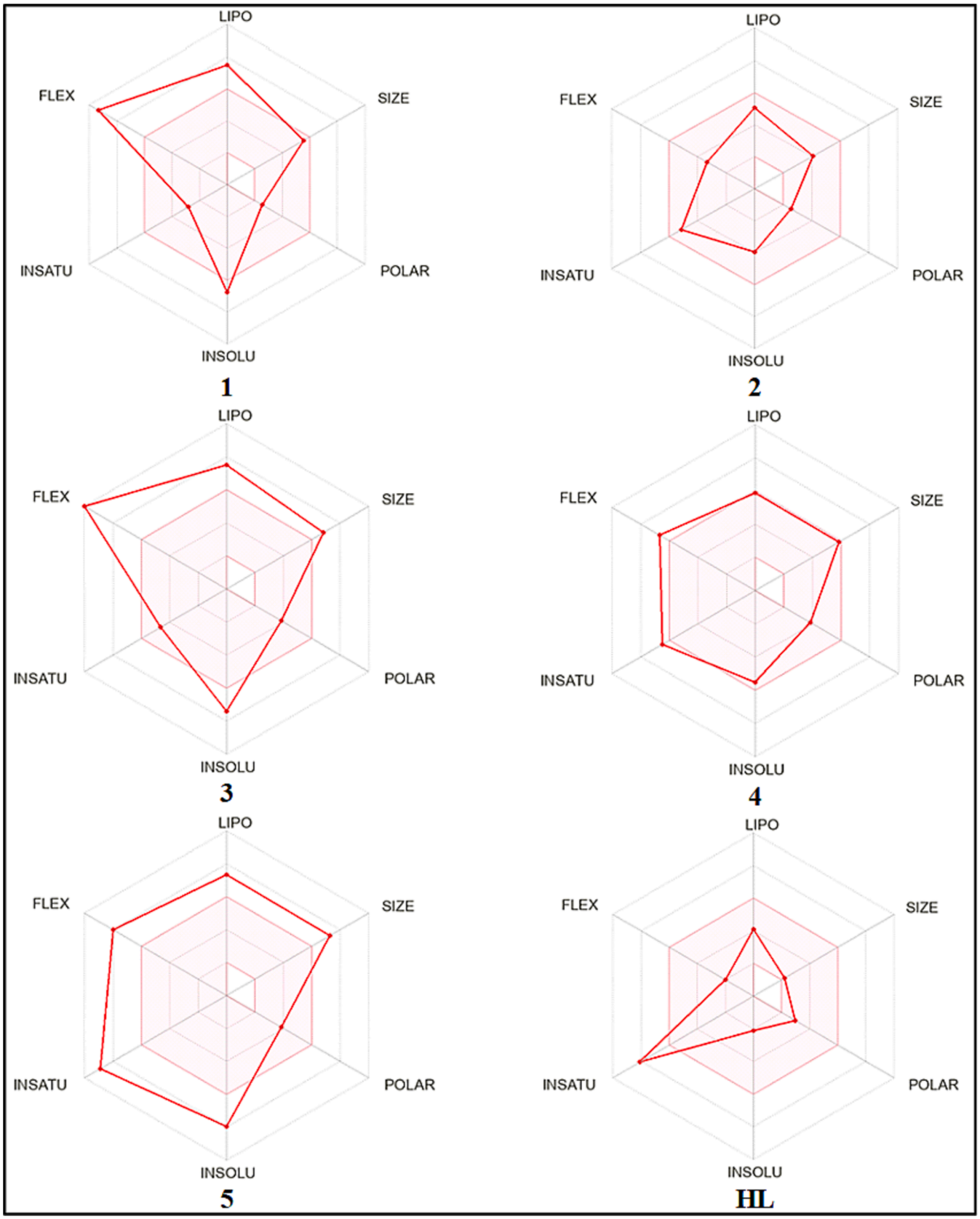

Fig. 20. Bioavailability radar image of **HL** and complexes **1**–**5**.

lipophilicity is –0.4 to 5.6. The logP values calculated from different drug-likeness filters for the synthesized compounds range from 1.55 to 4.85 which show that the tested compounds obey the drug recommended. The estimated aqueous-solubility, ESOL is an important parameter in drug development and its recommended range for a drug is 5–8. The ESOL value for **HL** & **2** lie in soluble class range while for **1**, **4** & **5** in the moderately soluble to poorly soluble range (Delaney, 2004).

The radar image (Fig. 20) consists of total 6 parameters; lipophilicity (LIPO: XLOGP3 between − 0.7 and + 5.0), molecular size (SIZE: MW between 150 and 500 g/mol), polarity (POLAR: tPSA between 20 and 130 $Å^2$), solubility (INSOLU: log(S) < 6), flexibility (FLEX: rotatable bonds < 9) and saturation (INSATU: Csp^3 > 0.25) (Daina et al., 2017, Daina,& Zoete, 2016, Hanifa et al., 2023, Hanifa et al., 2022). The pink area shows the optimal range for each property and enables a convenient summary of the drug-likeness of a molecule. The radar images for **HL** and **2** completely lie within the pink area (shown by red lines), indicating these are predicted to be orally bioavailable, while those for **HL** and **1** & **3**–**5** are marginally outside the pink range.

4. Conclusion

The condensation reaction of organotin(IV) chlorides with sodium-4-fluorophenoxyacetate salt in dry chloroform afforded di- and triorganotin(IV) carboxylates (**1**–**5**) in good yields with expected compositions as confirmed by the elemental analysis and NMR spectra. The carboxylate ligand in the complexes have shown bridging/chelating bidentate coordination mode as suggested by FT-IR spectra and confirmed by single crystal analysis for complexes **1**–**3**. Complexation has sufficiently improved the bioactivity of the carboxylate ligand. Complexes have shown activity in the selected enzymes inhibition assays in the order: Anti-Alzheimer's assay > anti-inflammatory assay > anti-diabetic assay. The higher activity of complex **3** (IC_{50} = 1.60 μg/mL) than standard (IC_{50} = 2.82 μg/mL) renders it a potential candidate for AChE inhibition and demands further studies. The complexes have shown different activity orders against the selected enzymes influenced by different controlling factors such as the number and nature of the tin-bonded alkyl groups, coordination number and geometry of the complexes. The synthesized complexes have also shown better anti-leishmanial activity than **HL**. Potential activity against brain cancer cell line (Malignant glioma U87) of complex **4** (IC_{50} = 12.54 ± 0.19 μg/mL), complex **5** (IC_{50} = 16.44 ± 0.17 μg/mL), and **HL** (IC_{50} = 21.95 ± 0.09 μg/mL) and low toxicity towards nonmalignant Human embryonic kidney HEK293 cells make these compounds good anticancer candidates for further studies. The multifaceted drug potential of the tested complexes was further strengthened by the higher antimicrobial activity of the complexes **1** and **2** compared to the standard drug Cefixime against *C. albicans* and *P. aeruginosa*, respectively.

CRediT authorship contribution statement

Shahnaz Rahim: Methodology, Visualization, Writing – original draft, Writing – review & editing. **Abdul Sadiq:** Investigation. **Aneela Javed:** Investigation. **Awal Noor:** Formal analysis, Software, Writing – original draft, Writing – review & editing. **Niaz Muhammad:** Conceptualization, Project administration, Resources, Supervision, Validation, Writing – original draft, Writing – review & editing. **Mohammad Ibrahim:** Investigation. **Sadaf Qayyum:** Formal analysis. **Khurshid Ayub:** Formal analysis, Software. **Nighat Fatima:** Investigation. **Sehrish Sarfaraz:** Formal analysis. **Mohammad Assad:** Investigation. **Maciej Kubicki:** Formal analysis, Software.

Acknowledgment

This work was supported by the Deanship of Scientific Research, Vice Presidency for Graduate Studies and Scientific Research, King Faisal University, Saudi Arabia (Grant No. 4759).

Appendix A. Supplementary data

Supplementary data to this article can be found online at https://doi.org/10.1016/j.arabjc.2024.105698.

References

Abbas, S., Ali, S., Khan, M.S., et al., 2013. Synthesis, crystal structure, enzyme inhibition, DNA protection, and antimicrobial studies of di- and triorganotin(IV) derivatives of 2-thiopheneacetic acid. J. Coord. Chem. 66 (15), 2765–2774. https://doi.org/10.1080/00958972.2013.815345.

Ahmad, S., Iftikhar, F., Ullah, F., et al., 2016. Rational design and synthesis of dihydropyrimidine based dual binding site acetylcholinesterase inhibitors. Bioorg. Chem. 69, 91–101. https://doi.org/10.1016/j.bioorg.2016.10.002.

Ahmad, G., Rasool, N., Rizwana, K., et al., 2019. Synthesis, in-vitro cholinesterase inhibition, in-vivo anticonvulsant activity and in-silico exploration of N-(4-methylpyridin-2-yl) thiophene-2-carboxamide analogs. Bioorg. Chem. 92, 103216 https://doi.org/10.1016/j.bioorg.2019.103216.

Ahmad, I., Rehman, Z., Waseem, A., et al., 2020. ORGANOTIN(IV) derivatives of amide-based carboxylates: synthesis, spectroscopic characterization, single crystal studies and antimicrobial, antioxidant, cytotoxic, anti-leishmanial, hemolytic, noncancerous, anticancer activities. Inorg. Chim. Acta 505, 119433. https://doi.org/10.1016/j.ica.2020.119433.

Ali, T., Muhammad, N., Ali, S., et al., 2021. Syntheses, crystal structures, antioxidant, in silico DNA and SARS-CoV-2 interaction studies of triorganotin(IV) carboxylates. J. Mol. Struct. 1234, 130190 https://doi.org/10.1016/j.molstruc.2021.130190.

Armarego, W., Chai, C., 2003. Purification of Laboratory Chemicals. Butterworth, Oxford.

Arshad, M.N., Asiri, A.M., Alamry, K.A., et al., 2015. Synthesis, crystal structure, spectroscopic and density functional theory (DFT) study of N-[3-anthracen-9-yl-1-(4-bromo-phenyl)-allylidene]-N-benzenesulfonohydrazine. Spectrochim. Acta - a: Mol. Biomol. Spectrosc. 142, 364–374. https://doi.org/10.1016/j.saa.2015.01.101.

Balouiri, M., Sadiki, M., Ibnsouda, S.K., 2016. Methods for in vitro evaluating antimicrobial activity: a review. J. Pharm. Anal. 6 (2), 71–79. https://doi.org/10.1016/j.jpha.2015.11.005.

Binda, C., Newton-Vinson, P., Hubálek, F., et al., 2002. Structure of human monoamine oxidase B, a drug target for the treatment of neurological disorders. Nat. Struct. Biol. 9, 22–26. https://doi.org/10.1038/nsb732.

Caricato, M., Frisch, Æ., Hiscocks, J., et al., 2009. Gaussian 09, IOps Reference. Gaussian, Inc. 340 Quinnipiac St., Bldg. 40 Wallingford, CT 06492 U.S.A.

Carradori, S., Silvestri, R., 2015. New frontiers in selective human MAO-B inhibitors: miniperspective. J. Med. Chem. 58, 6717–6732. https://doi.org/10.1021/jm501690r.

Daina, A., Michielin, O., Zoete, V., 2014. iLOGP: a simple, robust, and efficient description of n-octanol/water partition coefficient for drug design using the GB/SA approach. J. Chem. Inf. Model 54, 3284–3301. https://doi.org/10.1021/ci500467k.

Daina, A., Zoete, V., 2016. A boiled-egg to predict gastrointestinal absorption and brain penetration of small molecules. ChemMedChem 11, 1117–1121. https://doi.org/10.1002/cmdc.201600182.

Daina, A., Michielin, O., Zoete, V., 2017. SwissADME: a free web tool to evaluate pharmacokinetics, drug-likeness and medicinal chemistry friendliness of small molecules. Sci. Rep. 7, 1–13. https://doi.org/10.1038/srep42717.

Danish, M., Raza, M.A., Iftikhar, S., et al., 2020. Synthesis, single-crystal X-ray diffraction, and in vitro biological evaluation of sodium, cobalt, and tin complexes of o-nitro-/o-methoxyphenylacetic acid: experimental and theoretical investigation. Monatsh. Chem. 151 (11), 1727–1736. https://doi.org/10.1007/s00706-020-02699-y.

Debnath, P., Singh, K.S., Singh, K.K., et al., 2020. Di-BUTYLTIN(IV) complexes with azo-carboxylates: synthesis, characterization, crystal structures and their anti-diabetic assay. New J. Chem. 44, 5862–5872. https://doi.org/10.1039/D0NJ00536C.

Debnath, P., Debnath, P., Roy, S., et al., 2024. Azo-benzoic acid derivatives directed dinuclear and tetranuclear association of TRIMETHYLTIN(IV) complex components and their biological activities. Inorg. Chim. Acta 559, 121805. https://doi.org/10.1016/j.ica.2023.121805.

Delaney, J.S., 2004. ESOL: estimating aqueous solubility directly from molecular structure. J. Chem. Inf. Comput. 44, 1000–1005. https://doi.org/10.1021/ci034243x.

Eng, G., Song, X., Zapata, A., et al., 2007. Synthesis, structural and larvicidal studies of some triorganotin 2-(p-chlorophenyl)-3-methylbutyrates. J. Organomet. Chem. 692, 1398–1404. https://doi.org/10.1016/j.jorganchem.2006.11.030.

Fernandes, Q., Inchakalody, V.P., Bedhiafi, T., et al., 2024. Chronic inflammation and cancer; the two sides of a coin. Life Sci. 338, 122390, 10.1016/j.lfs.2023.122390.

Gul, R., Muhammad, N., Sirajuddin, M., et al., 2024. Design, physicochemical confirmation, single crystal structures as well as exploration of antibacterial and anticancer potential of organotin (IV) carboxylates. J. Mol. Struct. 1300, 137306 https://doi.org/10.1016/j.molstruc.2023.137306.

Hanifa, B., Sirajuddin, M., Tiekink, E.R.T., et al., 2022. Designing, physiochemical confirmation, evaluation of biological and in-silico potential of TRIORGANOTIN(IV) complexes. J. Mol. Struct. 1260, 132814 https://doi.org/10.1016/j.molstruc.2022.132814.

Hanifa, B., Bibi, N., Sirajuddin, M., et al., 2023. Synthesis, spectral characterization, biocidal investigation, in-silico and molecular docking studies of 4-[(2-chloro-4-methylphenyl) carbamoyl] butanoic acid derived triorganotin (IV) compounds.

J. Biomol. Struct. Dyn. 42 (4), 1826–1845. https://doi.org/10.1080/07391102.2023.2204160.
Hold, G.L., El-Omar, E.E., 2008. Genetic aspects of inflammation and cancer. Biochem. J. 410, 225–235. https://doi.org/10.1042/BJ20071341.
Holt, A., Sharman, D.F., Baker, G.B., et al., 1997. A continuous spectrophotometric assay for monoamine oxidase and related enzymes in tissue homogenates. Anal. Biochem. 244 (2), 384–392. https://doi.org/10.1006/abio.1996.9911.
Huneif, M.A., Alshehri, D.B., Alshaibari, K.S., et al., 2022. Design, synthesis and bioevaluation of new vanillin hybrid as multitarget inhibitor of α-glucosidase, α-amylase, PTP-1B and DPP4 for the treatment of type-II diabetes. Biomed. Pharmacother. 150, 113038, 10.1016/j.biopha.2022.113038.
Huneif, M.A., Fahad, S., et al., 2023. Antidiabetic, antihyperlipidemic, and antioxidant evaluation of phytosteroids from notholirion thomsonianum (royle) stapf. Plants 12 (20), 3591. https://doi.org/10.3390/plants12203591.
Hussain, S., Ali, S., Shahzadi, S., et al., 2015. Synthesis, characterization, biological activities, crystal structure and DNA binding of organotin(IV) 5-chlorosalicylates. J. Coord. Chem. 68 (14), 2369–2387. https://doi.org/10.1080/00958972.2015.1046849.
Hussain, S., Shujah, S., Rehman, A., et al., 2023. Synthesis, spectroscopic characterization, antileishmanial, DNA binding, antioxidant, cytotoxicity, antifungal and antibacterial studies of ORGANOTIN(IV) carboxylate complexes. Arab. J. Chem. 16, 105306 https://doi.org/10.1016/j.arabjc.2023.105306.
Joshi, R., Tomar, N., Pokharia, S., et al., 2023. Recent advancements in ORGANOTIN(IV) complexes of drugs: synthesis, characterization, and application. Results Chem. 5, 100955 https://doi.org/10.1016/j.rechem.2023.100955.
Kasalović, M.P., Jelača, S., Maksimović-Ivanić, D., et al., 2024. Novel DIPHENYLTIN(IV) complexes with carboxylato N-functionalized 2-quinolone ligands: synthesis, characterization and in vitro anticancer studies. J. Inorg. Biochem. 250, 112399 https://doi.org/10.1016/j.jinorgbio.2023.112399.
Khan, R., Naureen, H., Javed, A., et al., 2023. Alocasia odora–mediated synthesis of silver nanoparticles, their cytotoxicity, and virucidal potential. Appl. Microbiol. Biotechnol. 107 (1), 111–123. https://doi.org/10.1007/s00253-022-12298-y.
Kovala-Demertzi, D., Dokorou, V., Ciunik, Z., et al., 2002. Organotin mefenamic complexes—preparations, spectroscopic studies and crystal structure of a triphenyltin ester of mefenamic acid: novel anti-tuberculosis agents. Appl. Organomet. Chem. 16(7), 360–368. 10.1002/aoc.308.
Kuete, V., Kamga, J., Sandjo, L.P., et al., 2011. Antimicrobial activities of the methanol extract, fractions and compounds from Ficus polita vahl. (moraceae). BMC Complement Altern. Med. 11, 6. https://doi.org/10.1186/1472-6882-11-6.
Lipinski, C.A., Lombardo, F., Dominy, B.W., et al., 1997. Experimental and computational approaches to estimate solubility and permeability in drug discovery and development settings. Adv. Drug Deliv. Rev. 23 (1–3), 3–25. https://doi.org/10.1016/S0169-409X(96)00423-1.
Lobo, S., 2020. Is there enough focus on lipophilicity in drug discovery? Expert Opin. Drug Discov. 15 (3), 261–263. https://doi.org/10.1080/17460441.2020.1691995.
Lockhart, T.P., Manders, W.F., 1986. Inorg. Chem. 25, 892–895. https://doi.org/10.1021/ic00227a002.
Luo, Y.H., Wu, G.G., Mao, S.L., et al., 2013. Complexation of different metals with a novel N-donor bridging receptor and hirshfeld surfaces analysis. Inorg. Chim. Acta 397, 1–9. https://doi.org/10.1016/j.ica.2012.11.010.
Mahnashi, M.H., Alqahtani, Y.S., Alqarni, A.O., et al., 2021. Crude extract and isolated bioactive compounds from notholirion thomsonianum (royale) stapf as multitargets antidiabetic agents: in-vitro and molecular docking approaches. BMC Complement. Med. Ther. 21, 1–13. https://doi.org/10.1186/s12906-021-03443-7.
Mahnashi, M.H., Alyami, B.A., Alqahtani, Y.S., et al., 2022. Antioxidant molecules isolated from edible prostrate knotweed: rational derivatization to produce more potent molecules. Oxid. Med. Cell. Longev. 2022, 3127480. https://doi.org/10.1155/2022/3127480.
Mahon, M.F., Molloy, K.C., Stanley, J.E., et al., 2005. Atmospheric pressure deposition of fluorine-doped SnO2 thin films from organotin fluorocarboxylate precursors. Appl. Organomet. Chem. 19, 658–671. https://doi.org/10.1002/aoc.722.
Mkrtchyan, S., Jakubczyk, M., Lanka, S., et al., 2021. Mechanochemical transformation of CF3 group: synthesis of amides and schiff bases. Adv. Synth. Catal. 363 (24), 5448–5460. https://doi.org/10.1002/adsc.202100538.
Muhammad, N., Shah, A., Shuja, S., et al., 2009. ORGANOTIN(IV) 4-nitrophenylethanoates: synthesis, structural characteristics and intercalative mode of interaction with DNA. J. Organomet. Chem. 694, 3431–3437. https://doi.org/10.1016/j.jorganchem.2009.06.036.
Muhammad, N., Ikram, M., Perveen, F., et al., 2019. 2019b. syntheses, crystal structures and DNA binding potential of copper(II) carboxylates. J. Mol. Struct. 771–782 https://doi.org/10.1016/j.molstruc.2019.07.014.
Muhammad, N., Ahmad, M., Sirajuddin, M., et al., 2022. Synthesis, characterization, biological activity and molecular docking studies of novel organotin(IV) carboxylates. Front. Pharmacol. 13, 864336 https://doi.org/10.3389/fphar.2022.864336.
Muhammad, N., Shah, N.A., Ali, S., et al., 2018. Antimicrobial efficiency of diorganotin (IV) bis-[3-(4-chlorophenyl)-2-methylacrylate]. J. Coord. Chem. 71(20), 3315–3329. 10.1080/00958972.2018.1513131.
Muhammad, N., Shah, N.A., Ali, S., et al., 2019a. Theoretical and Experimental in vitro Antifungal and Antitumor Activities of Organotin (IV) Derivatives of 3-(4-nitrophenyl)-2-methylacrylic acid. Pharm. Chem. J. 53, 689–696. 10.1007/s11094-019-02064-2.
Munir, A., Khusha, A., Saeed, K., et al., 2020. Synthesis, in-vitro, in-vivo anti-inflammatory activities and molecular docking studies of acyl and salicylic acid hydrazide derivatives. Bioorg. Chem. 104, 104168. 10.1016/j.bioorg.2020.104168.
Naz, N., Sirajuddin, M., Haider, A., et al., 2019. Synthesis, characterization, biological screenings and molecular docking study of ORGANOTIN(IV) derivatives of 2,4-dichlorophenoxyacetic acid. J. Mol. Struct. 1179, 662–671. https://doi.org/10.1016/j.molstruc.2018.11.011.
Noor, A., 2022. Crystallographic evidence of η1-coordination of bulky aminopyridine in halide-containing IRON(II) complexes. Crystals 12 (5), 697. https://doi.org/10.3390/cryst12050697.
Ojo, O.A., Nwafor-Ezeh, P.I., Rotimi, D.E., et al., 2023. M. Apoptosis, inflammation, and oxidative stress in infertility: A mini review. Toxicol. Rep.10, 448–462. 10.1016/j.toxrep.2023.04.006.
Pantelić, N.Đ., Božić, B., Zmejkovski, B.B., et al., 2021. In vitro evaluation of antiproliferative properties of novel ORGANOTIN(IV) carboxylate compounds with propanoic acid derivatives on a panel of human cancer cell lines. Molecules 26, 3199. https://doi.org/10.3390/molecules26113199.
Rahim, H., Sadiq, A., Khan, S., et al., 2019. Fabrication and characterization of glimepiride nanosuspension by ultrasonication-assisted precipitation for improvement of oral bioavailability and in vitro α-glucosidase inhibition. Int. J. Nanomed. 14, 6287–6296. https://doi.org/10.2147/IJN.S210548.
Rahman, T.U., Arfan, M., Mahmood, T., et al., 2015. Isolation, spectroscopic and density functional theory studies of 7-(4-methoxyphenyl)-9H-furo [2, 3-f] chromen-9-one: A new flavonoid from the bark of Millettia ovalifolia. Spectrochim. Acta - A: Mol. Biomol. Spectrosc. 146, 24–32. https://doi.org/10.1016/j.saa.2015.03.061.
Retz, W., Gsell, W., Münch, G., et al., 1998. Free radicals in alzheimer's disease. J. Neural Transm. Suppl. 54, 221–236. https://doi.org/10.1007/978-3-7091-7508-8_22.
Rizzo, M., Andersona, S.W., Dawsonc, J., et al., 2000. Vision and cognition in Alzheimer's disease. Neuropsychologia 38 (8), 1157–1169. https://doi.org/10.1016/s0028-3932(00)00023–3.
Romero-Cháveza, M.M., Pineda-Urbinaa, K., Pérezb, D.J., et al., 2018. Organotin(IV) compounds derived from ibuprofen and cinnamic acids, an alternative into design of anti-inflammatory by the cyclooxygenases (COX-1 and COX-2) pathway. J. Organomet. Chem. 862, 58–70. https://doi.org/10.1016/j.jorganchem.2018.02.049.
Salmon, J.A., Higgs, G.A. 1987. Prostaglandins and leukotrienes as inflammatory mediators. Br. Med. Bull. 43, 285–296. 10.1093/oxfordjournals.bmb.a072183.
Sarfaraz, S., Yar, M., Ayub, K., 2022a. Covalent triazine framework (CTF-0) surface as a smart sensing material for the detection of CWAs and industrial pollutants. Mater. Sci. Semicond. 139, 106334, 10.1016/j.mssp.2021.106334.
Sarfaraz, S., Yar, M., Khan, A.A., et al., 2022b. DFT investigation of adsorption of nitro-explosives over C2N surface: highly selective towards trinitro benzene. J. Mol. Liq. 352, 118652, 10.1016/j.molliq.2022.118652.
Sarotti, A.M., Pellegrinet, S.C., 2012. Application of the multi-standard methodology for calculating ^{1}H NMR chemical shifts. J. Org. Chem. 77 (14), 6059–6065. https://doi.org/10.1021/jo3008447.
Sheldrick, G.M., 2015a. SHELXT–INTEGRATED space-group and crystal-structure determination. Acta Cryst. A71, 3–8. https://doi.org/10.1107/S2053273314026370.
Sheldrick, G.M., 2015b. Crystal structure refinement with SHELXL. Acta Cryst. C71, 3–8. https://doi.org/10.1107/S2053229614024218.
Sirajuddin, M., Ali, S., Mckee, V., et al., 2019. Exploration of ORGANOTIN(IV) derivatives for medicinal applications: synthesis, spectroscopic characterization, structural elucidation and molecular docking study. J. Mol. Struct. 1181, 93–108. https://doi.org/10.1016/j.molstruc.2018.12.041.
Su, M., Hu, R., Tang, T., et al., 2023. Review of the correlation between chinese medicine and intestinal microbiota on the efficacy of diabetes mellitus. Front. Endocrinol. 13, 2022. https://doi.org/10.3389/fendo.2022.1085092.
Tariq, M., Sirajuddin, M., Ali, S., et al., 2016. J. Photochem. photobiol. B, Biol. 158, 174–183. https://doi.org/10.1016/j.jphotobiol.2016.02.028.
Technologies, A., 2018. CrysAlis PRO (version 1.171.39.46). Agilent Technologies Ltd.
Thomas, T., 2000. Monoamine oxidase-B inhibitors in the treatment of Alzheimers disease. Neurobiol. Aging 21, 343–348. 10.1016/s0197-4580(00)00100-7.
Tiekink, E.R.T., 1994. The rich diversity in tin carboxylate structures. Trends Organomet. Chem. 1 (1), 71–116.
Turner, M.J., McKinnon, J.J., Wolff, S.K., et al., 2017. Crystal Explorer 17. University of Western Australia, Pert, WA, Australia.
Viola, Muhammad, N., Khan, I.N., et al., 2022. Synthesis, characterization, antioxidant, antileishmanial, anticancer, DNA and theoretical SARS-CoV-2 interaction studies of copper(II) carboxylate complexes. J. Mol. Struct. 1253 (21), 132308, 10.1016/j.molstruc.2021.132308.
Walters, W.P., Murcko, M.A., 2002. Prediction of 'drug-likeness'. Adv. Drug Deliv. Rev. 54, 255–271. https://doi.org/10.1016/s0169-409x(02)00003–0.
Waring, M.J., 2010. Lipophilicity in drug discovery. Expert Opin. Drug Discov. 5 (3), 235–248. https://doi.org/10.1517/17460441003605098.
Youdim, M.B.H., Edmondson, D., Tipton, K.F., 2006. The therapeutic potential of monoamine oxidase inhibitors. Nat. Rev. Neurosci. 7, 295–309. https://doi.org/10.1038/nrn1883.
Yousaf, A., Waseem, M., Javed, A., et al., 2022. Augmented anticancer effect and antibacterial activity of silver nanoparticles synthesized by using Taxus wallichiana leaf extract. PeerJ. 10, e14391. https://doi.org/10.7717/peerj.14391.
Zghair, K.H., Sahez, E.J., Al-Qadhi, B.N., 2016. Antiparasitic effect of carbonnanotubes on Leishmania donovani in vitro. Iraqi J. Sci. 57 (4B), 2641–2649.